Supporting Information

Enhancing Local K^+ Adsorption by High-density Cube Corners for Efficient Electroreduction of CO_2 to C_{2+} Products

Hu Zang[1], Changjiang Liu[1], Qinyuan Ji[1], Jiahao Wang[1], Haiyan Lu[1], Nan Yu[1], and Baoyou Geng[1,2]*

[1]College of Chemistry and Materials Science, The key Laboratory of Functional Molecular Solids, Ministry of Education, The Key Laboratory of Electrochemical Clean Energy of Anhui Higher Education Institutes, Anhui Provincial Engineering Laboratory for New-Energy Vehicle Battery Energy-Storage Materials, Anhui Normal University, Jiuhua Road 189, Wuhu, 241002, China.

[2]Institute of Energy Hefei Comprehensive National Science Center Hefei, 230031, China.

*Correspondence to: bygeng@mail.ahnu.edu.cn

Table of Contents

Section 1. Materials and Methods

1.1. Chemicals and Materials. Copper nitrate trihydrate (99%, $Cu(NO_3)_2 \cdot 3H_2O$, AR) and potassium bicarbonate (99.9%, $KHCO_3$) were supplied by Shanghai Macklin Biochemical Technology Co., Ltd.; Ethylene glycol (99.5%, EG, AR), dimethyl sulfoxide (99.9%, DMSO) and anhydrous ethanol (99.7%, AR) were purchased from Sinopharm Chemical Reagent Co., Ltd.; D_2O (99.99%) and potassium hydroxide (95%, KOH) were bought from Shanghai Aladdin Biochemical Technology Co., Ltd.; Nafion solution (5%), carbon paper (SGL-28BC) and anion exchange membrane (N117) were supplied by Suzhou Sinero Technology Co., Ltd.; Carbon black (VXC-72) was bought from Shanghai Cabot Chemical Co., Ltd.; Ar (99.999%), CO (99.999%) and CO_2 (99.999%) were supplied by Xuancheng Liyuan Gas Co., Ltd.; Deionized water (Provided by the laboratory, 18.25 MΩ cm^{-1}). All materials do not require further purification when used.

1.2. Synthesis of Cu_2O-X. Referring to the solvent method for the preparation of Cu_2O microspheres by Chen et al.[1] In a typical synthesis, firstly, 40 mL of EG and 483.2 mg of $Cu(NO_3)_2 \cdot 3H_2O$ were added into a 50 mL beaker, magnetic stirred until $Cu(NO_3)_2 \cdot 3H_2O$ was completely dissolved. Then X mL of H_2O was added, magnetic stirred for 2 h at room temperature. Finally, the liquid was poured into a 70 mL high-pressure reactor, which was sealed and then transferred to an oven. The oven kept at 180 °C for 1 h. After the high-pressure reactor was cooled down, the samples were washed with H_2O and ethanol for 3 times and centrifuged to remove the EG from the surface of the products. Dry the washed sample in a vacuum oven for 12 hours at 60 °C and set it aside. Because different volumes of water were used in this experiment, the samples were named Cu_2O-X, and X was the volume of water in the experiment, which was 0, 0.5, 1, 2, 4, and 10 mL. So the samples were named as Cu_2O-0, Cu_2O-0.5, Cu_2O-1, Cu_2O-2, Cu_2O-4, and Cu_2O-10, respectively.

Section 2. Simulation and Characterizations

2.1. COMSOL Multiphysics Simulations. The finite element method (FEM) simulation was carried out using COMSOL multiphysics 6.1 software based on steady state current physical field on the surface of electrodes modified with cubic corners. In the simulation, five different electrode surface simulation geometries (Figure S1) were constructed based on 3D space. The performance of the five models in electrolytes was simulated and calculated using the electric currents (ec) and transport of diluted species (tds) physics modules in COMSOL multiphysics, coupling with the steady-state

current physical field in the ACDC module, and simulated on micro local surfaces based on Ohm's law. The Ohm's law conservation equation is as follows:

$$J = \sigma E + J_e \tag{1}$$

where **J** represents the current density, **E** represents the electric field, σ is the material conductivity, and $\mathbf{J}_e$ is the external current density.

Continuity equation for ionic current density:

$$i = -F\sum - z_i^2 m_i F c_i \nabla \emptyset_l \tag{2}$$

where **i** represents the current density vector; i represents the ionic potential, z_i is the ion charge; m_i is the mobility, c_i is the ion concentration, and F is the Faraday constant.

In terms of diffusion mass transfer, the distribution of K^+ is dynamically balanced by the combined action of electric field and ion diffusion, follows the material transfer equation and Nernst Planck equation:

$$-D\nabla C - zmFc\nabla \emptyset_l = N \tag{3}$$

where D is the diffusivity, c represents the ion concentration, z is the valence, m is the mobility, $\emptyset_l$ is the ionic potential, **N** is the ionic flux.

A geometry in a localized square space at a microscopic scale is constructed in the simulation. The relative tolerance in the steady-state solver was set to 0.01. For the boundary condition setting, a V=0 zero potential boundary is set in the bottom region and the top is set as V_{top}=0.1 mV potential boundary. For the material setting, the conductivity of the electrolyte was 4.5 S/m. The ion diffusion coefficient was set to be $1 \times e^{-9}$ m^2/s, and the ion ambient concentration was set to be 1 mol/L.

2.2. Materials characterizations. The morphology and structure of the catalysts were described using scanning electron microscopy (SEM, Hitachi S-8100), transmission electron microscopy (TEM, Hitachi HT-7700) and high-resolution mission electron microscope (HRTEM, Tecnai G220 FEI). Information on the crystal structure of the catalysts was collected using X-ray powder diffraction (XRD, SmartLab 9kw Bruker) with Cu Kα in the 2θ range 10~80°. The valence states of the elements on the catalysts surface were analyzed using X-ray photoelectron spectroscopy (XPS, ESCALAB 250XI Thermo Fisher). Gas products of CO_2RR were analyzed simultaneously using a GC 9790 II (Fuli) gas chromatograph. Liquid products were detected by 400 M NMR (ASCEndtm400 Bruker). In-situ Raman (inViainVia Raman) and in-situ FT-IR (INVENIO-

RINVENIO-R Bruker) monitoring of the reaction process.

2.3. Double Layer Capacitance (C_{dl}) Measurement. The C_{dl} of the catalysts was tested by cyclic voltammetry in a flow cell under the same conditions as CO_2 electroreduction. The catalysts were tested using cyclic voltammetry in the non-Faraday region 0.1 ~ 0.2 V vs. RHE at different scan rates, the difference in current density (Δj) was recorded for different catalysts. C_{dl} was estimated by plotting Δj for different scan rates at 0.15 V vs. RHE. The linear slope is equal to twice the C_{dl}.[2] The electrochemical active area (ECSA) and roughness factor (R_f) of the catalyst material were calculated using the double layer capacitance method.[3-5]

2.4. K^+ Adsorption Experiment. As shown in Figure S23, the catalysts were placed in 0.1 M $KHCO_3$ solution and applied a constant voltage, and after running for 120 s at -1.2 V vs. RHE. The electrode was removed from the $KHCO_3$ solution, after removing the voltage, the electrode was placed into 10 mL of pure water and shaken for 60 s. The above procedure was repeated for 10 times, then the inductively coupled plasma optical emission spectrometer (ICP-MS: Thermo Fisher iCAP RQ) was used to measure the K^+ concentration in 10 mL of pure water. The K^+ concentration adsorbed in 0.1 M $KHCO_3$ solution at the working electrode without voltage was used as the blank background. The final K^+ concentration after deducting the blank background represents the adsorption capacity of K^+ on the catalyst surface.[6]

2.5. CO Adsorption Experiment. CO adsorption experiments were carried out on the catalyst surface using a homemade device to investigate the CO adsorption capacity of the samples (Figure S24). First, the prepared catalyst electrode (1×1 cm^2) was connected to an electrochemical workstation (CHI 760e) and placed in a sealed container. This hermetically sealed container was connected to a vacuum pump and a CO gas cylinder, and the vacuum state of the hermetically sealed container was maintained by the operation of the vacuum pump before the test was carried out. The current versus time profile was monitored by multistep potentials under vacuum, with 0 V, -0.2 V, and -0.4 V (vs. RHE) potentials applied to the electrodes and run for 20 s at each potential. The CO gas was then filled into the sealed vessel and the same electrochemical test procedure as under vacuum was performed. Due to the adsorption of CO on the catalyst surface, the magnitude of the current tested in the two states changed, and the calculation of the difference between the current densities of the two states at each potential ($\Delta j = j_{co}$-j_{vacuum}) can reflect the adsorption capacity of the catalyst surface for CO.[6,7]

2.6. In-situ Raman Measurements. As shown in Figure S29, measurements were performed using inViainVia Raman microscopy in a modified flow cell. Carbon paper (SGL-28BC) coated with catalyst ink was the working electrode, Pt and Ag/AgCl electrode wire were counter and reference electrodes, respectively. The flow rate of 1 M KOH electrolyte was 10 mL min^{-1} in the cathode and anode chambers, the flow rate of CO_2 in the gas chamber was 100 sccm. The signals of 0 to -1.0 V vs. RHE were recorded using a 785 nm laser with 20 s integration and averaging of two scans.

2.7. In-situ FT-IR measurements. In-situ FT-IR field tests were performed by an INVENIO R FT-IR (Bruker) spectrometer with a CHI 760e electrochemical workstation. Figure S32 was the schematic of electrolytic cell for in-situ FT-IR test. The working electrode was prepared by coating catalyst ink on a polished glassy carbon electrode, Ag/AgCl electrode and Pt wire were used as reference and counter electrodes, respectively. The electrolyte was a 0.5 M $KHCO_3$ solution saturated with CO_2 in advance, and CO_2 gas was continuously introduced. The spectra collection started at the potential of 0 V vs. RHE and then jumped to -1.0 V vs. RHE. The scan time was 10 s per curve and the spectral resolution was 4 cm^{-1}. All spectra are expressed in terms of absorbance. The scan rate was 20 khz.

2.8. DFT Theoretical Calculations. DFT calculation using the Vienna Ab-inito Simulation package (VASP).[8,9] The Perdew Burke Ernzerhof (PBE) functional is used to describe exchange related effects in the Generalized Gradient Approximation (GGA) method.[10,11] Calculating core-valence interactions using the Projection Enhanced Wave (PAW) method.[12] 3×3×1 Monkhorst-Pack grid k-points were used to sample the Brillouin zone integration, the value of energy cutoff for plane wave expansion was 480 eV.

Calculating the adsorption energy using the formula (4):

$$Eads = E(A+B) - E(A) - E(B) \tag{4}$$

where Eads and E(A+B) is the adsorption energy and the adsorption configuration calculated energy, respectively. E(A) and E(B) is the calculated energy of substrate and adsorbent, respectively.

The ΔG of each step is calculated by the formula (5):

$$\Delta G = \Delta E + \Delta ZPE - T\Delta S \tag{5}$$

where ΔG and ΔE is the Gibbs free energy change and the electronic energy difference by DFT calculations, respectively. ΔZPE and ΔS is the zero-point energy change and the entropy change,

respectively. T is 298.15 K (this work).

After frequency calculation, ZPE can be obtained from the formula (6):[13]

$$ZPE = \frac{1}{2}\sum hvi \tag{6}$$

The adsorbed species TS value are calculated according to the formula (7):[14]

$$TS = k_B T\left[\sum_k ln\left(\frac{1}{1-e^{-hv/k_B T}}\right) + \sum_k \frac{hv}{k_B T}\frac{1}{\left(e^{hv/k_B T}-1\right)} + 1\right] \tag{7}$$

Section 3. Electrochemical CO_2RR Performance Evaluation

3.1. Preparation of working electrode. The catalyst ink was prepared by adding 5 mg of catalyst, 1 mg of VXC-72 C, and 20 μL of Nafion solution (5% wt%) to 480 μL of ethanol for 30 min of ultrasonic dispersion. Catalyst ink was sprayed onto carbon paper (SGL-28BC) with a spray gun and the SGL-28BC was dried under an infrared light lamp. The dried working electrode was used for subsequent electrochemical testing experiments.

3.2. Electrocatalytic CO_2 reduction. Electrocatalytic CO_2 reduction studies were carried out on the catalyst using a flow cell. CO_2 was reduced electrochemically using a CHI 760e electrochemical workstation, which was equipped with a CHI 680c high-current amplifier. The equation E (vs. RHE) = E (vs. Ag/AgCl) + 0.197 V + 0.0591 × pH relationship was utilized to convert all potentials to the RHE reference scale. Cu_2O-0 was firstly tested for linear sweep voltammetry (LSV) under N_2 and CO_2 atmosphere, and the other Cu_2O-X was tested for LSV under CO_2 atmosphere. The CO_2 electroreduction properties of the Cu_2O-X catalysts were then tested by the chronopotentiometric method in a flow cell in 1 M KOH, and a peristaltic pump was used to circulate the electrolyte through the cathode and anode chambers, respectively. The flow rate of CO_2 in the gas chamber was controlled using a digital gas flow controller AST-10.

3.3. Gas and liquid product analysis. The gas and liquid products of CO_2RR were analyzed using a GC 9790 II (Fuli) and 400 M NMR (Bruker), respectively.

Calculation of Faradaic efficiency (FE). The calculation of FE for gas products was performed using following equation:[15,16]

$$FE = \frac{n \cdot F \cdot ppm \cdot G \cdot P}{R \cdot T \cdot I} \tag{8}$$

where *n* represents the electrons transferred from CO_2 (i.e., 2 for CO, 8 for CH_4, and 12 for C_2H_4)

and H_2O (i.e., 2 for H_2) to the product formation, *F* represents Faraday's constant (96485 $C \cdot mol^{-1}$), *ppm* represents the product concentration were measured using GC; *G* is gas flow rate, *P*=1.01 x 10^5 Pa, *R*=8.314 $J \cdot mol^{-1} \cdot K^{-1}$, *T*=298.15 K. *I* is the current.

The FE for liquid products were calculated by the formula (9):[17]

$$FE = \frac{n \cdot F \cdot M \cdot V}{Q} \tag{9}$$

where *n* represents the electrons transferred from CO_2 (i.e., 2 for $HCOO^-$, 8 for CH_3COO^-, 12 for CH_3CH_2OH, and 18 for PrOH), *F* is Faraday's constant (96485 $C \cdot mol^{-1}$), *V* represents the volume of the liquid, *M* represents the molar concentration of the liquid product, *Q* is the total charge passing through the liquid in a given analysis time.

Section 4. Additional Figures and Tables

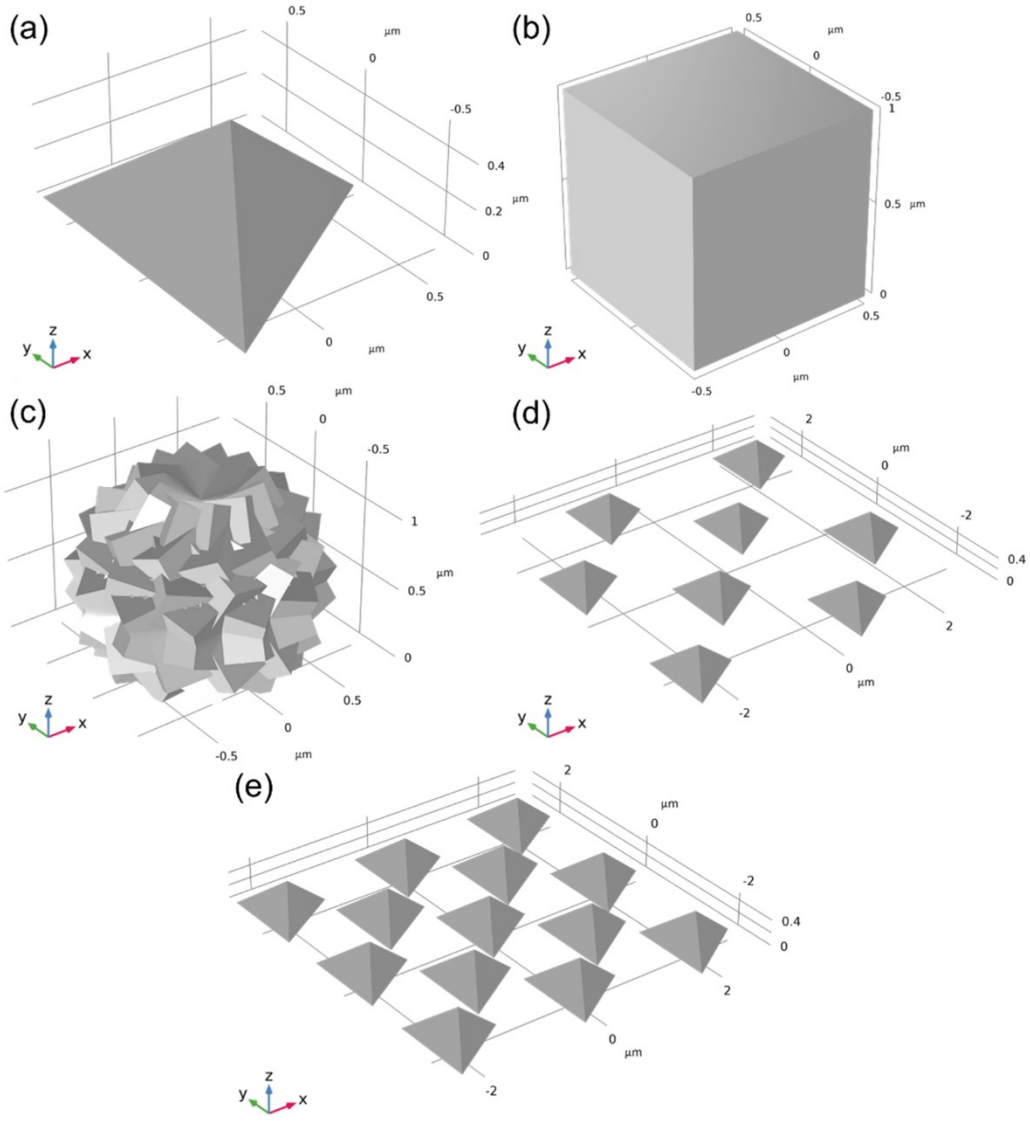

Figure S1. The original 3D models of M1 (a), M2 (b), M3 (c), M4 (d) and M5 (e) by COMSOL multiphysics simulations.

As shown in the Figure S1 above, we simulated five models using COMSOL multiphysics field simulation: a single cube corner, a cube, a microsphere composed of multiple cube corners, 8 and 13 cube corners on the same plane, named M1, M2, M3, M4 and M5, respectively. where M1-3 represent models with different spatial structures and densities of cube corners, and M4-5 represent models with different densities of cube corners on the same plane. Different numbers of cube corners on the same plane represent cube corners of different densities.

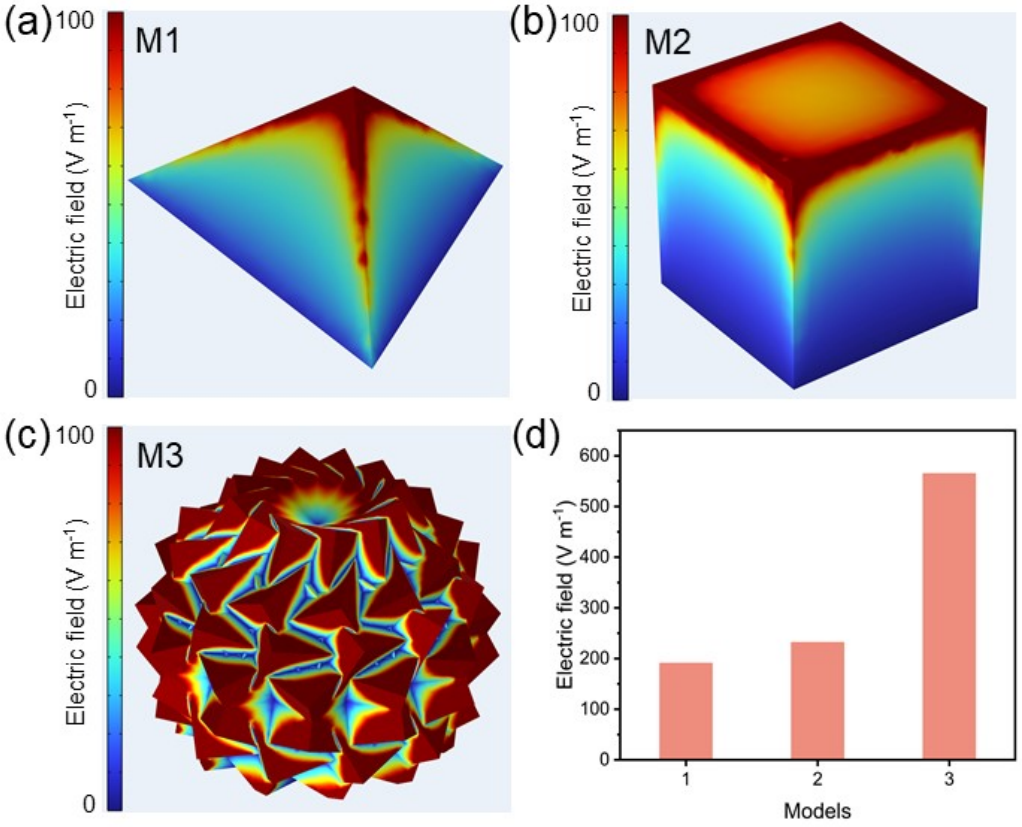

Figure S2. The electric field distribution on M1 (a), M2 (b) and M3 (c) through COMSOL multiphysics simulations. (d) The value of electric field on the cube corners surfaces of M1, M2 and M3.

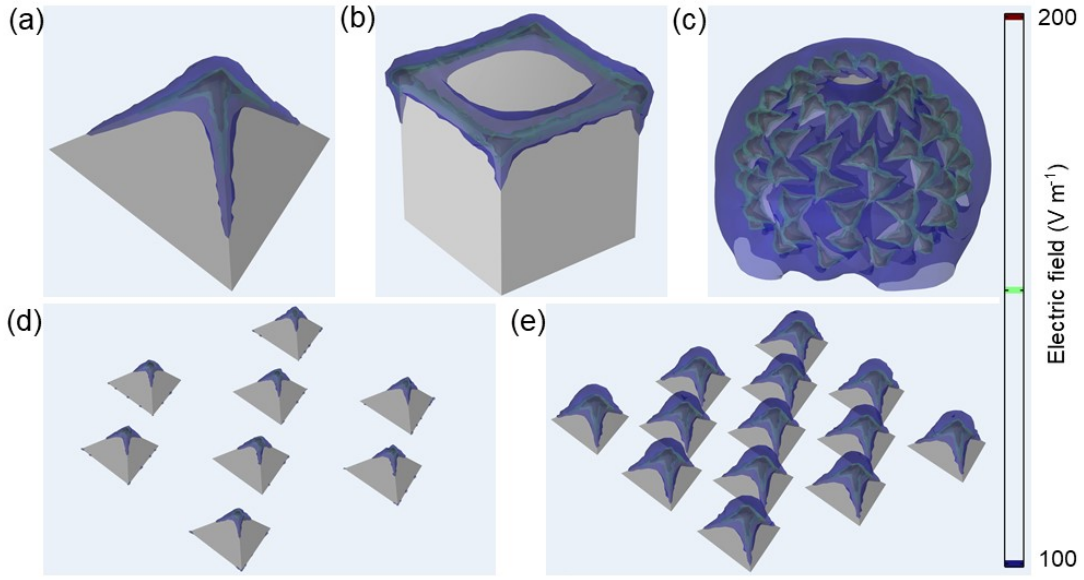

Figure S3. The isosurfaces of electric field distribution on M1 (a), M2 (b), M3 (c), M4 (d) and M5 (e) through COMSOL multiphysics simulations.

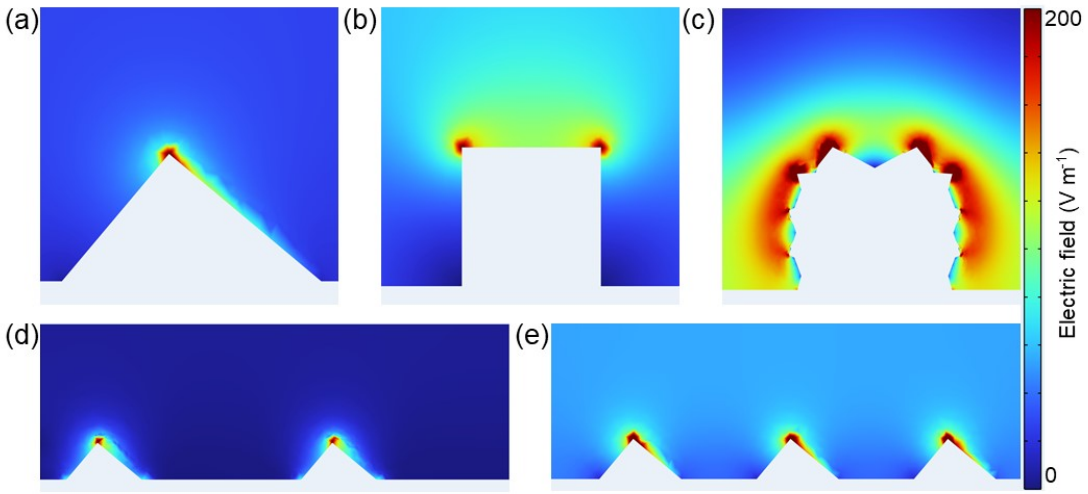

Figure S4. The sections of electric field distribution on M1 (a), M2 (b), M3 (c), M4 (d) and M5 (e) through COMSOL multiphysics simulations.

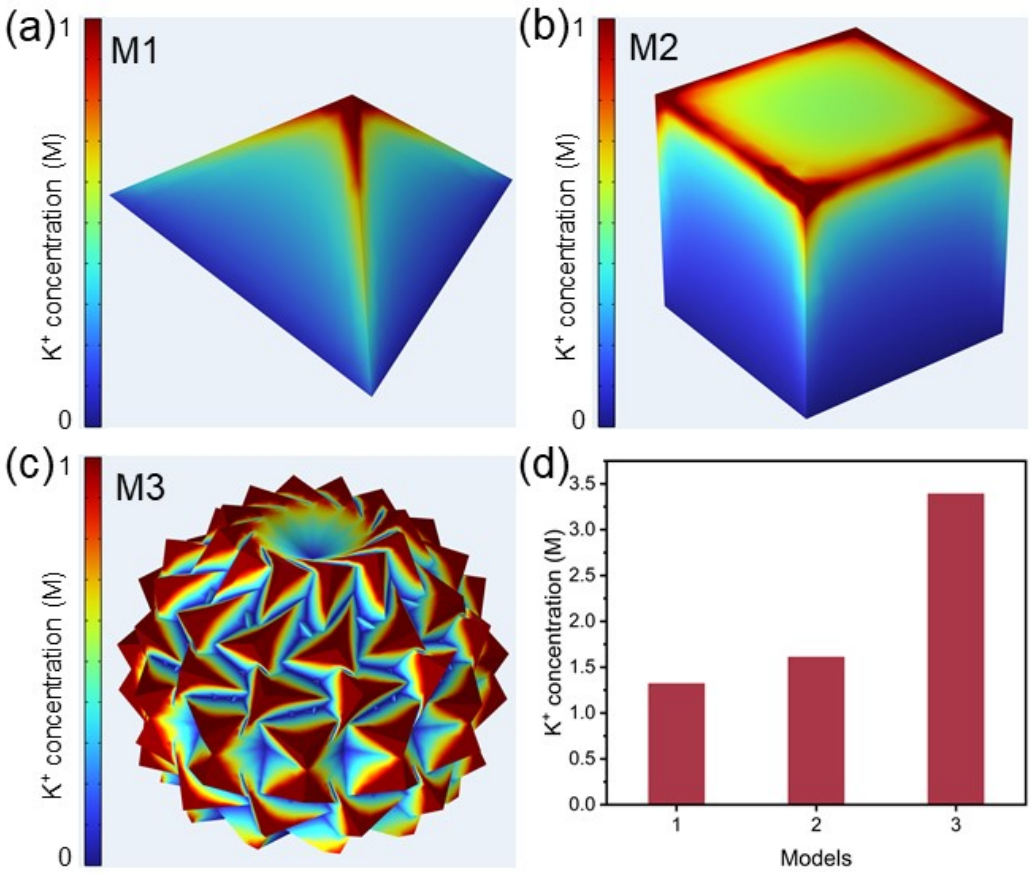

Figure S5. K^+ concentration distribution on M1 (a), M2 (b) and M3 (c) through COMSOL multiphysics simulations. (d) The K^+ concentration on the cube corners surfaces of M1, M2 and M3.

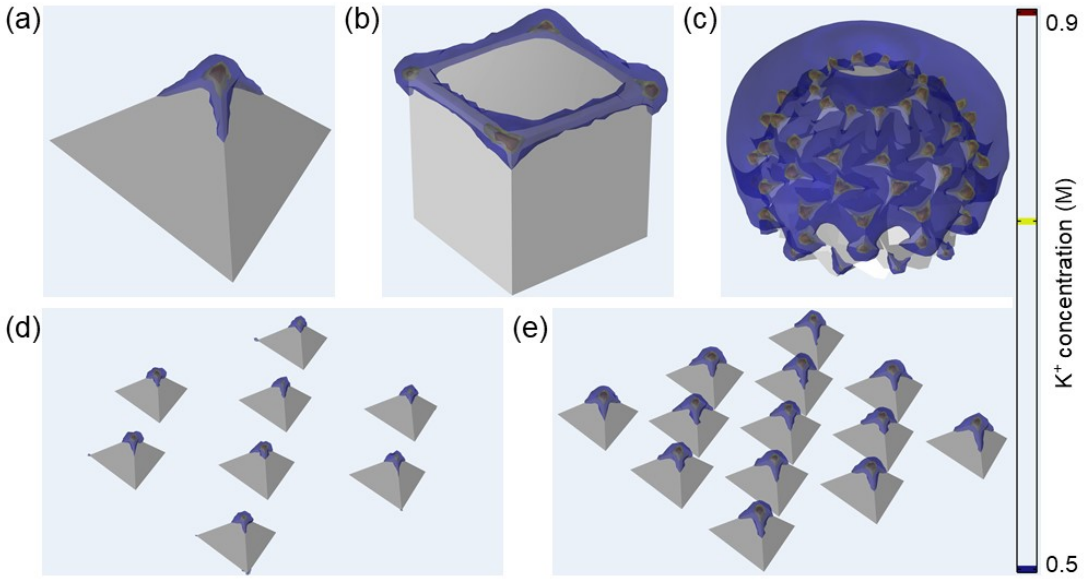

Figure S6. The isosurfaces of K^+ concentration distribution on M1 (a), M2 (b), M3 (c), M4 (d) and M5 (e) through COMSOL multiphysics simulations.

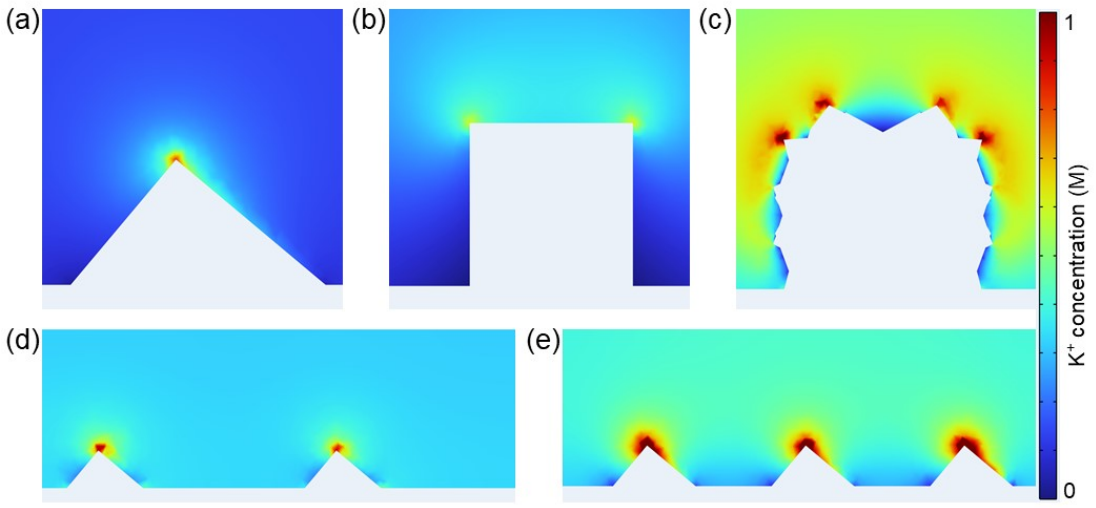

Figure S7. The sections of K^+ concentration distribution on M1 (a), M2 (b), M3 (c), M4 (d) and M5 (e) through COMSOL multiphysics simulations.

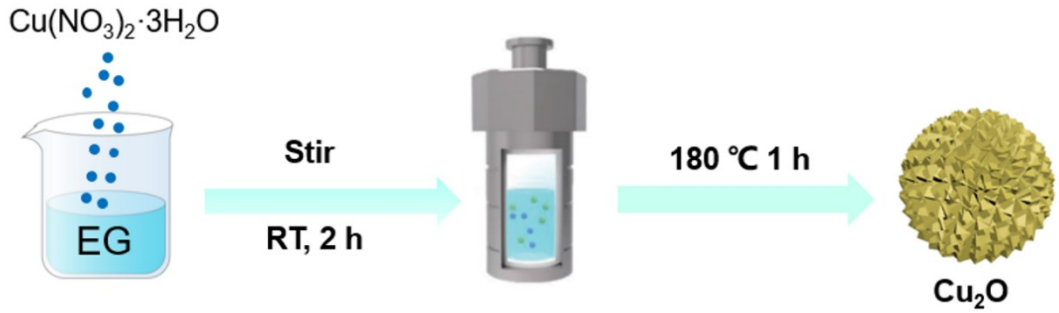

Figure S8. Schematic illustration the synthetic process of Cu_2O-0 microsphere.

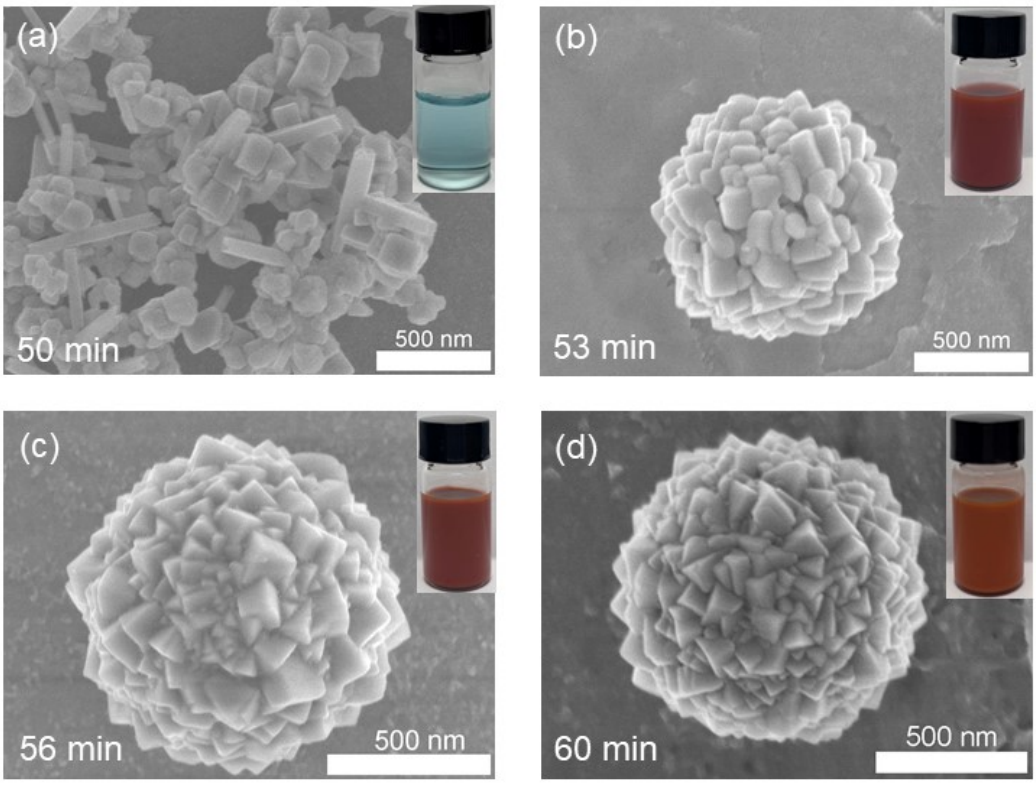

Figure S9. The SEM images for the formation process of the Cu_2O-0 microspheres: (a) 50 min, (b) 53 min, (c) 56 min, and (d) 60 min. The inserts are the corresponding photos of the samples, respectively.

As the heating time proceeded, the color of the solution and the morphology of sample gradually changed. When $Cu(NO_3)_2 \cdot 3H_2O$ was dissolved in ethylene glycol, the solution shows a transparent blue color. When the heating time proceeded to 50 min, the solution was light blue. After centrifugal drying, many nanoparticles which were mainly cubic in shape were found. During 53-60 min, the color of the solution changed significantly, but it was mainly dominated by brick red, and the morphology also changed. When the reaction proceeded to 53 min, many cubes aggregated to form microspheres. The dimensions of the Cu_2O microspheres did not change significantly during 53-60 min, but the vertices and ridges of the cubic corners of the Cu_2O microsphere surface became more pronounced, while the density of the cubic corners increased.

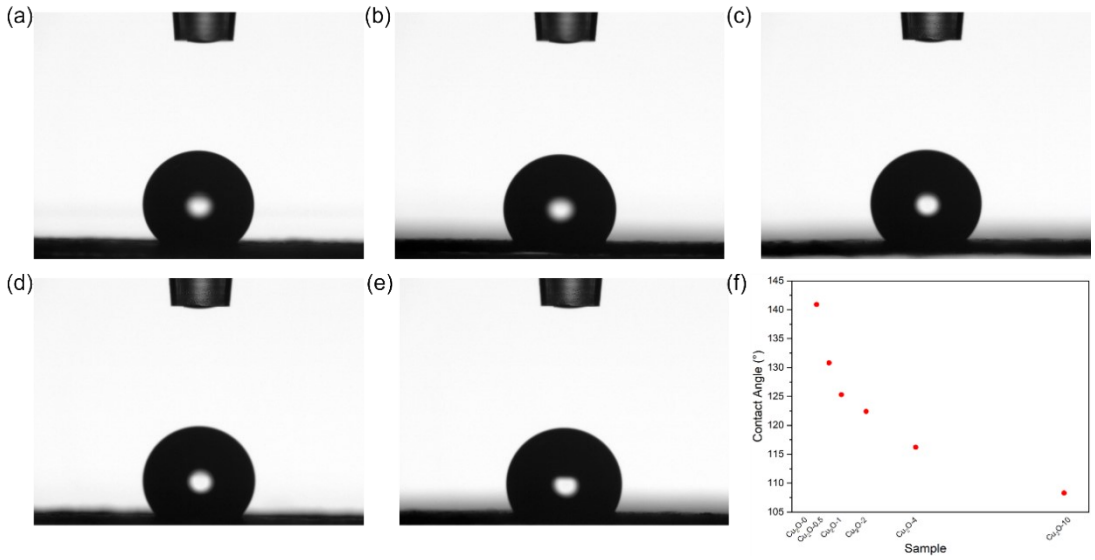

Figure S10. The air/water contact angles of the Cu_2O-X catalysts. (a) Cu_2O-0.5. (b) Cu_2O-1. (c) Cu_2O-2. (d) Cu_2O-4. (e) Cu_2O-10. (f) Comparison of the air/water contact angles of Cu_2O-X catalysts.

Figure S10 shows that the air/water contact angle of Cu_2O-X gradually decreased with the increase of water addition during the synthesis of Cu_2O-X, and the air/water contact angle of Cu_2O-10 was minimized to 108°. The hydrophobicity of Cu_2O-X catalysts may be related to the density and size of the cubic corners on their microsphere surfaces, with higher densities and smaller sizes resulting in greater hydrophobicity.

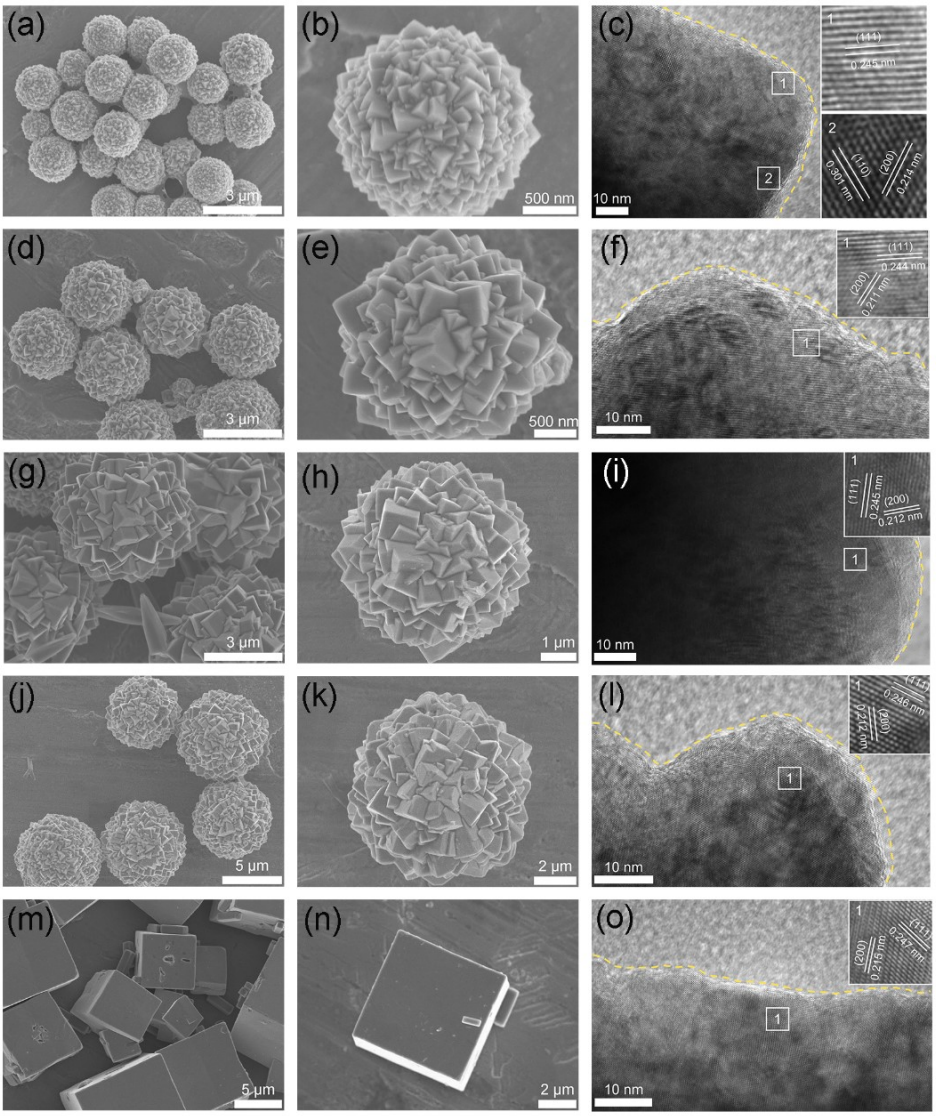

Figure S11. SEM and HRTEM images of Cu_2O-X catalysts. (a), (b) and (c) Cu_2O-0.5. (d), (e) and (f) Cu_2O-1. (g), (h) and (i) Cu_2O-2. (j), (k) and (l) Cu_2O-4. (m), (n) and (o) Cu_2O-10.

The morphology of Cu_2O-X did not change significantly with increasing water content and had the same crystalline surface (Cu_2O (200), (111), and (110)); however, the size of Cu_2O microspheres gradually became larger, and the density of cubic inflection on the surface of the Cu_2O microspheres gradually became smaller. When the water content was increased to 10 mL, Cu_2O was no longer microspheres but cubes. This is may be due to the fact that the excess water led to a decrease in the viscosity of the solution, which destabilized the microspheres and ultimately led to the formation of only microcubic particles.

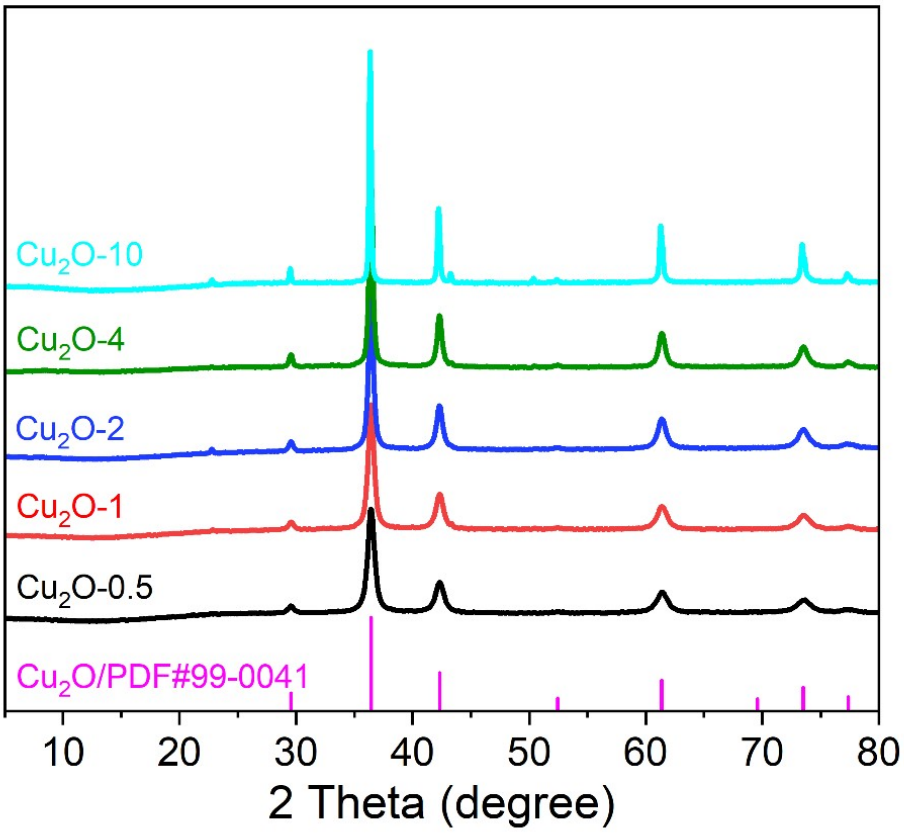

Figure S12. Powder XRD patterns of Cu_2O-X and standard Cu_2O (JCPDS: PDF#99-0041).

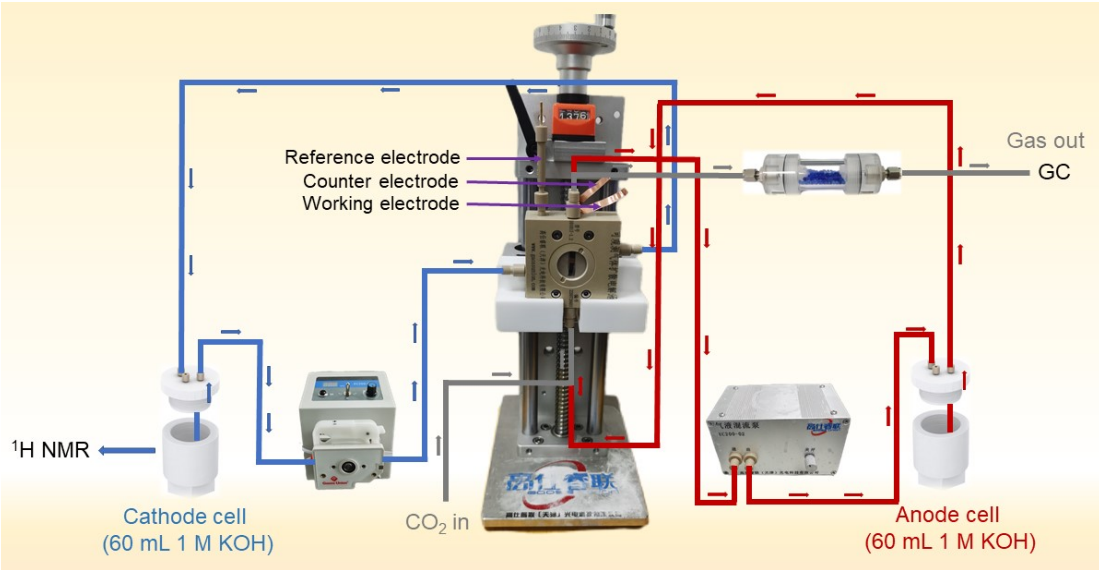

Figure S13. Schematic diagram of flow-through electrolytic cell.

The CO_2 electroreduction performance of Cu_2O-X catalysts were studied by flow cell. The schematic diagram of the CO_2RR device is shown in Figure S13, which is composed of a flow cell, a peristaltic pump, a liquid flow pool, etc. The flow cell includes a cathode chamber, an anode chamber and a gas chamber. In the CO_2RR experiment, the cathode chamber and anode chamber are separated by an anion exchange membrane N117, and 1 M KOH electrolyte is circulated in the cathode chamber and anode chamber using a peristaltic pump. The digital gas flow controller AST-10 is used to control the flow rate of CO_2 in the gas chamber. Meanwhile, Ag/AgCl and Pt sheets were used as reference electrode and counter electrode, respectively.

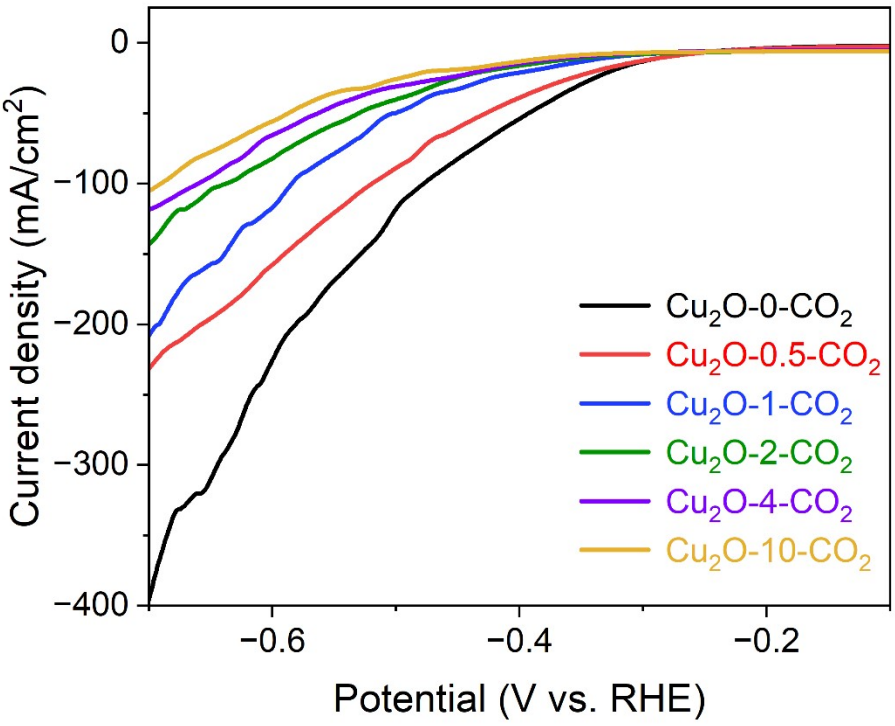

Figure S14. LSV curves of Cu_2O-X catalysts with CO_2 atmosphere.

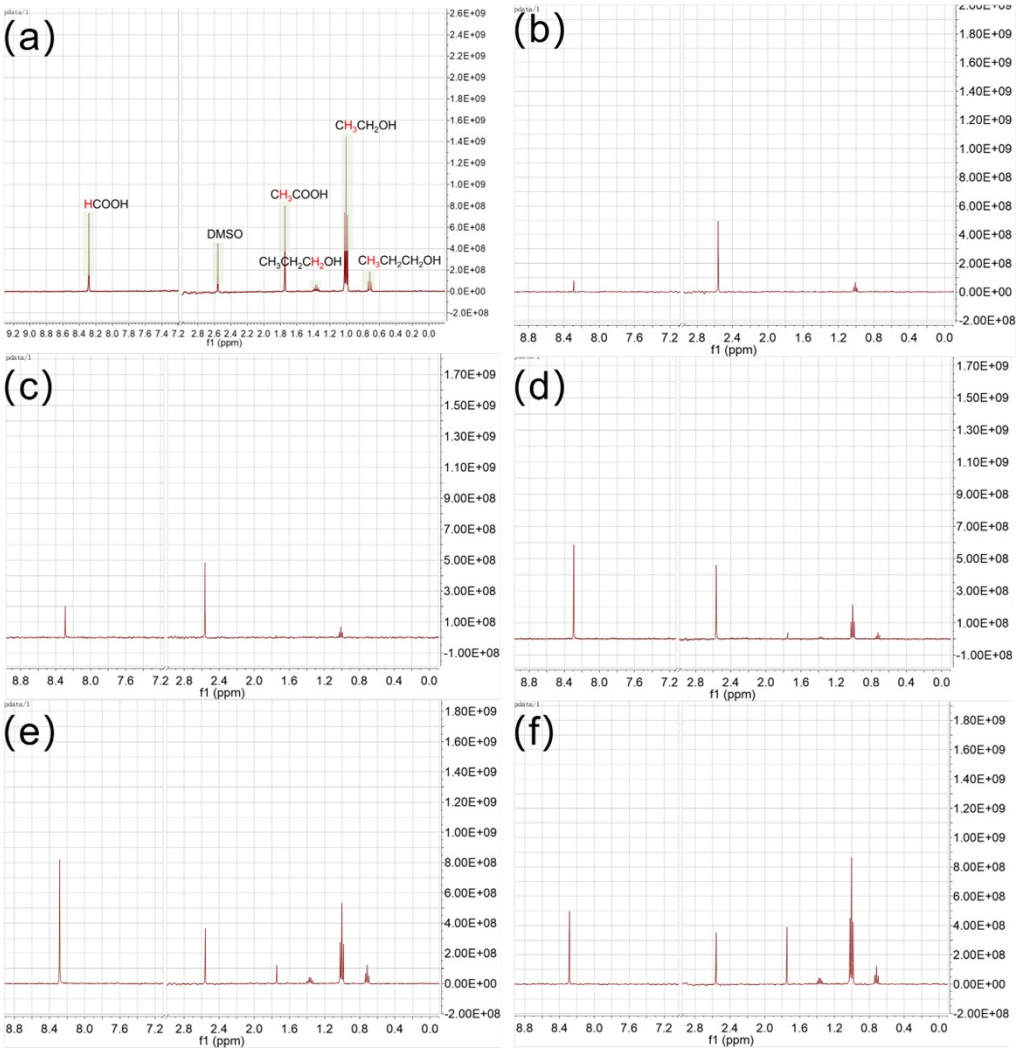

Figure S15. ^{1}H NMR spectra after CO_2RR. (a) A representative ^{1}H NMR spectrum after CO_2RR. Liquid products ^{1}H NMR spectra of the electroreduction of CO_2 over Cu_2O-0 catalyst at current densities of (b) 100 mA, (c) 200 mA, (d) 500 mA, (e) 600 mA, and (f) 700 mA, respectively.

The ^{1}H NMR spectra of the reduction products are shown in Figure S15a, the liquid phase products are mainly HCOOH, CH_3COOH, CH_3CH_2OH and PrOH. The ^{1}H NMR spectra of the electrocatalytic CO_2 reduction products of the Cu_2O-0 catalyst at different current densities (Figure S15b-f).

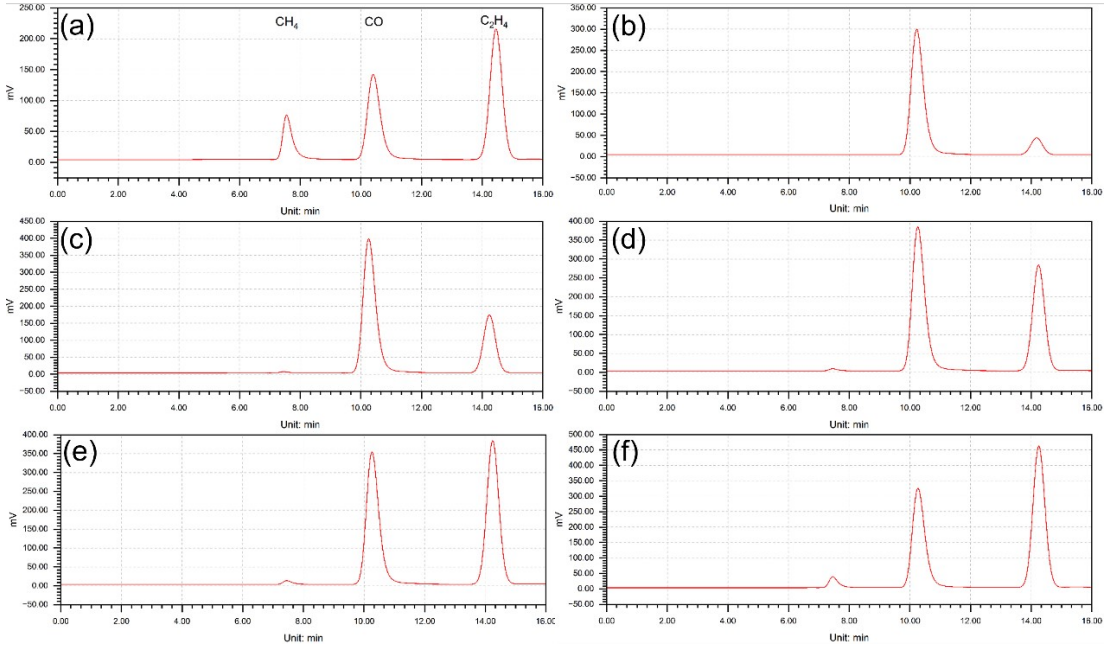

Figure S16. The FID spectra of GC after CO_2RR. (a) A representative FID spectrum after CO_2RR. The gas products in GC spectra of the electroreduction of CO_2 over Cu_2O-0 catalyst at current densities of (b) 100 mA, (c) 200 mA, (d) 500 mA, (e) 600 mA, and (f) 700 mA, respectively.

The FID spectra of GC in Figures S16a show that the gas-phase products are mainly CH_4 CO and C_2H_4. The FID spectra of the electrocatalytic CO_2 reduction products of the Cu_2O-0 catalyst at different current densities (Figure S16b-f).

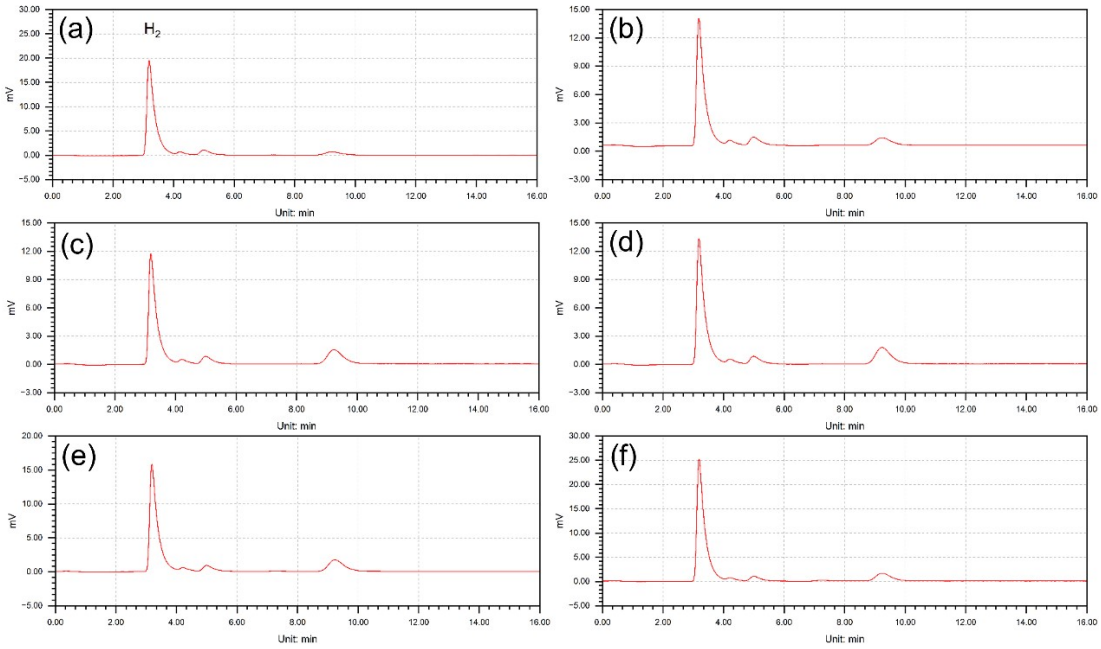

Figure S17. The TCD spectra of GC after CO_2RR. (a) A representative TCD spectrum after CO_2RR. H_2 product in GC spectra of the electroreduction of CO_2 over Cu_2O-0 catalyst at current densities of (b) 100 mA, (c) 200 mA, (d) 500 mA, (e) 600 mA, and (f) 700 mA, respectively.

The TCD spectra of GC in Figures S17a show that the gas-phase products is H_2. The TCD spectra of the electrocatalytic CO_2 reduction products of the Cu_2O-0 catalyst at different current densities (Figure S17b-f).

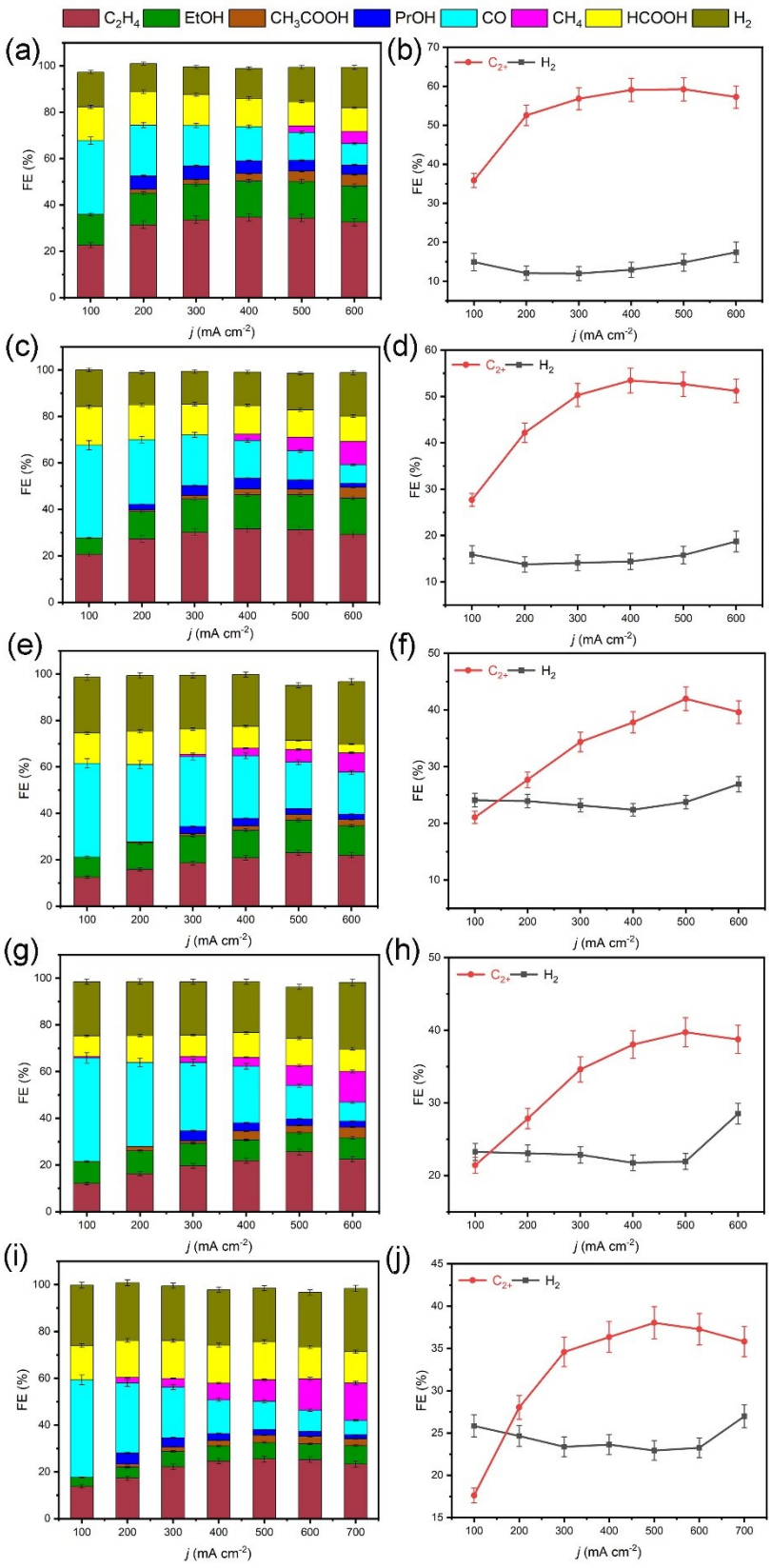

Figure S18. FEs of various products on the Cu_2O-X catalysts during CO_2RR at different current densities. (a) and (b) Cu_2O-0.5. (c) and (d) Cu_2O-1. (e) and (f) Cu_2O-2. (g) and (h) Cu_2O-4. (i) and (j) Cu_2O-10.

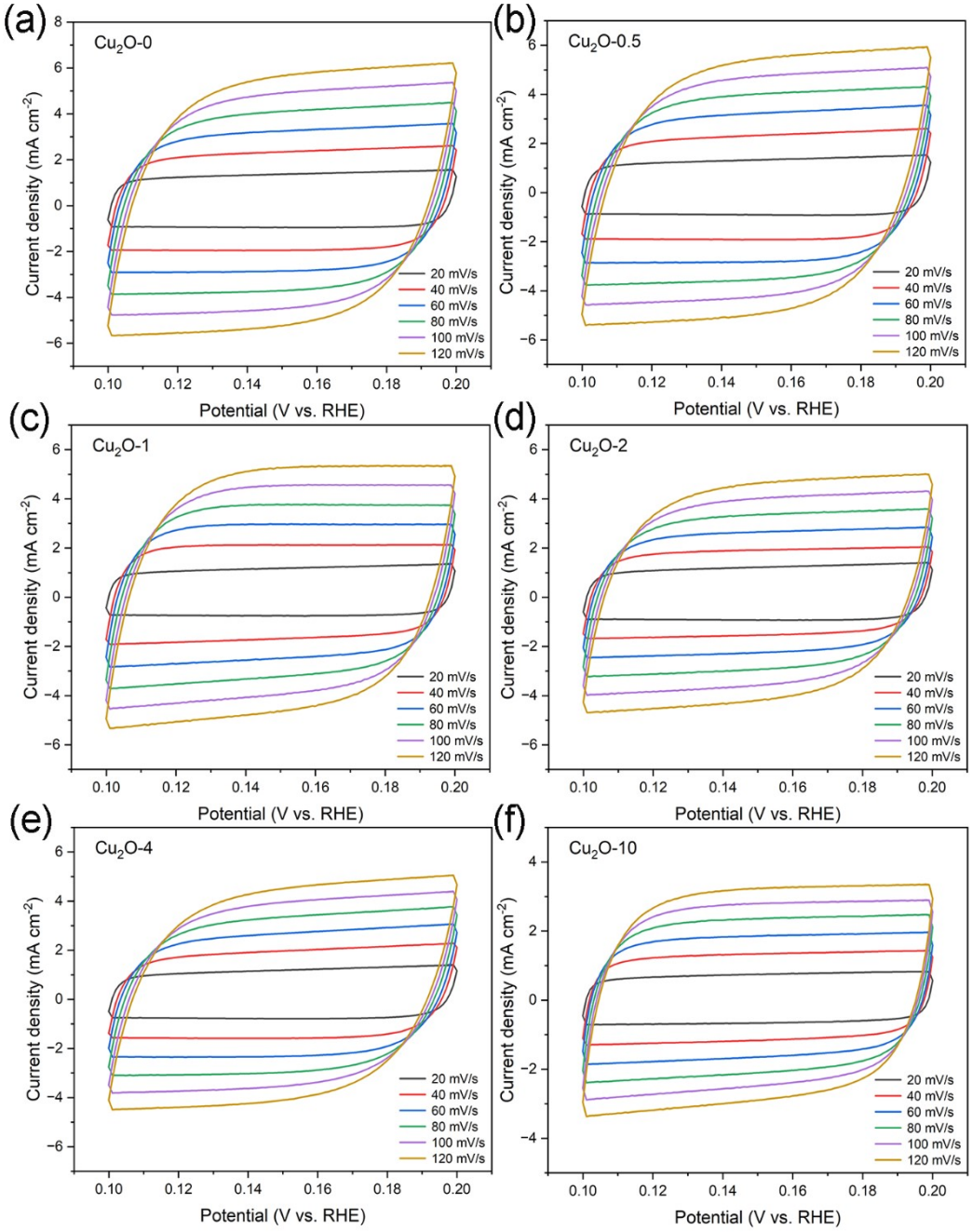

Figure S19. Cyclic voltammograms of Cu_2O-X catalysts in 1 M KOH scanned from 0.1 to 0.2 V vs. RHE at different scan rates. (a) Cu_2O-0. (b) Cu_2O-0.5. (c) Cu_2O-1. (d) Cu_2O-2. (e) Cu_2O-4. (f) Cu_2O-10.

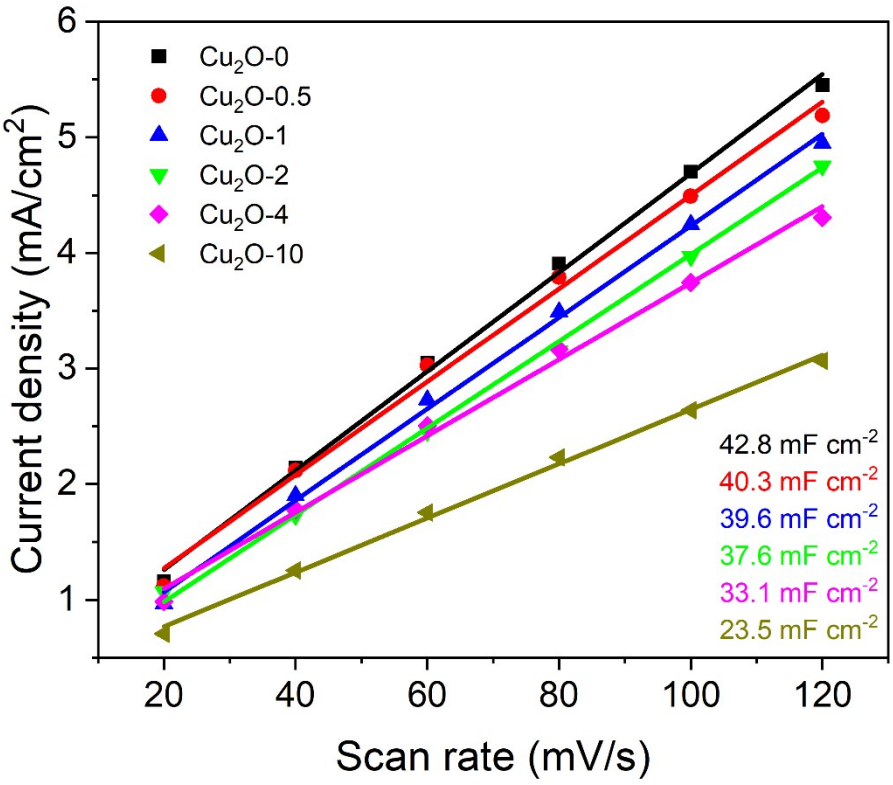

Figure S20. The determination of double layer capacitance for Cu_2O-X catalysts.

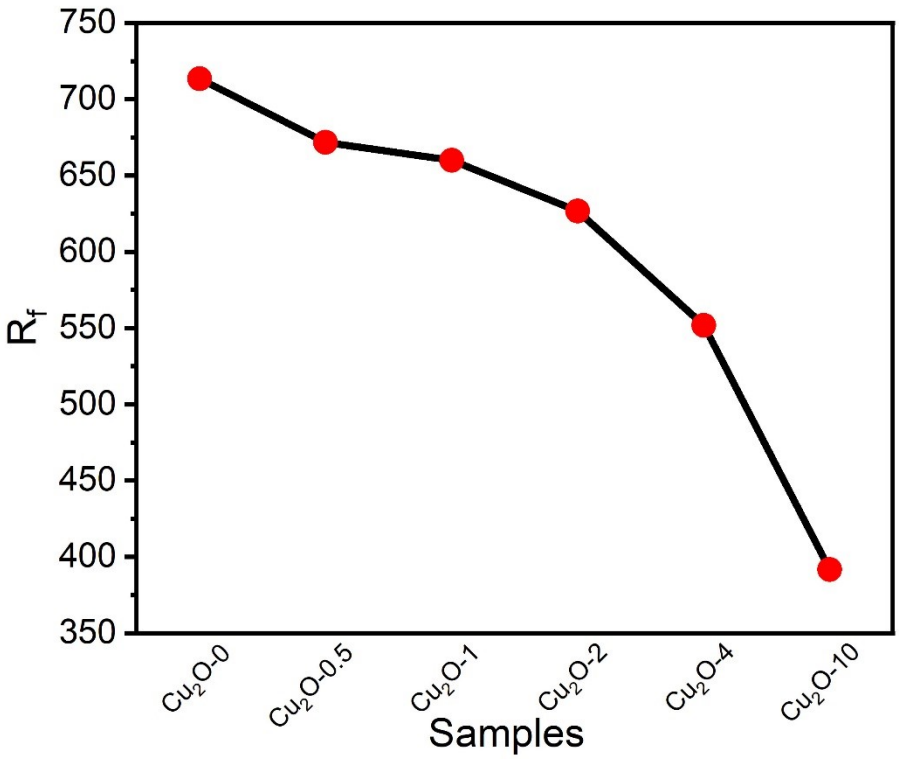

Figure S21. Surface roughness factor (R_f) of Cu_2O-X catalysts.

R_f can not only illustrate the roughness situation of Cu_2O-X surface, but also illustrate the density magnitude of the cubic corners on the surface of Cu_2O-X microspheres from the side, which may be due to the fact that the roughness of the surface of Cu_2O-X microspheres is mainly constituted by the cubic corners. A larger R_f indicates a rougher Cu_2O-X surface and a higher density of cubic corners on the microsphere surface, thus exposing more vertices (Cu_2O (111)) and ridges (Cu_2O (110)).

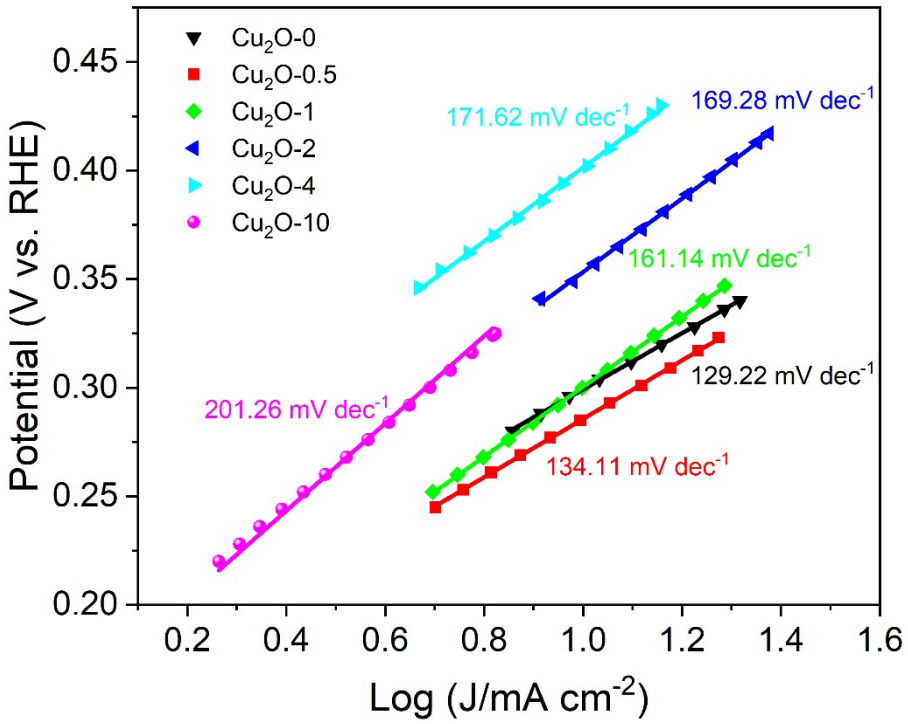

Figure S22. Tafel slopes for Cu_2O-X catalysts.

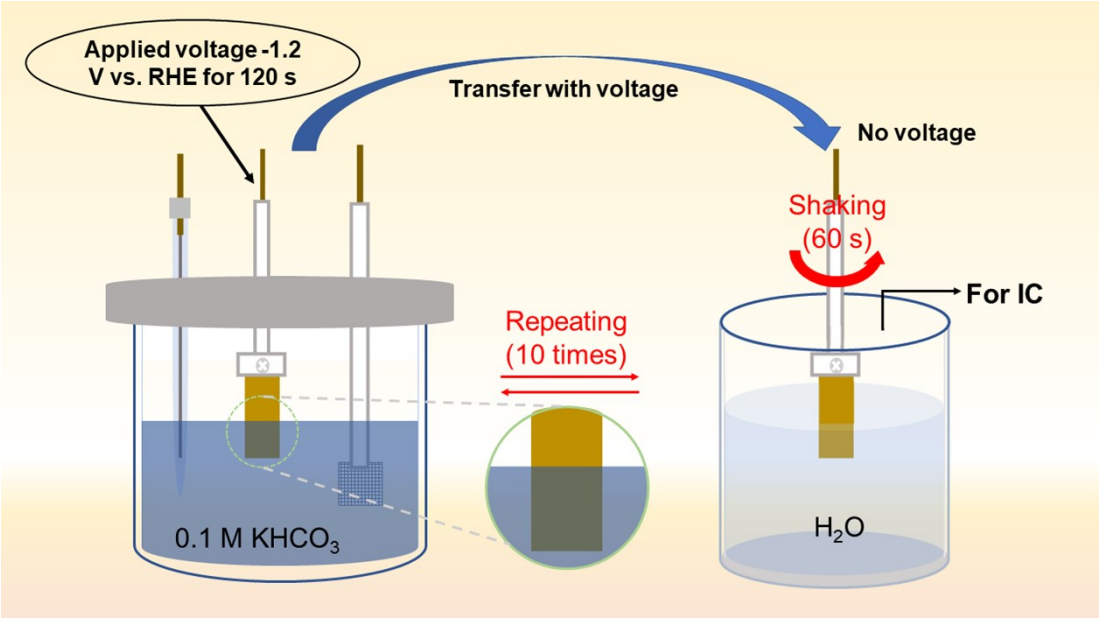

Figure S23. Schematic diagram of K^+ adsorption experiment.

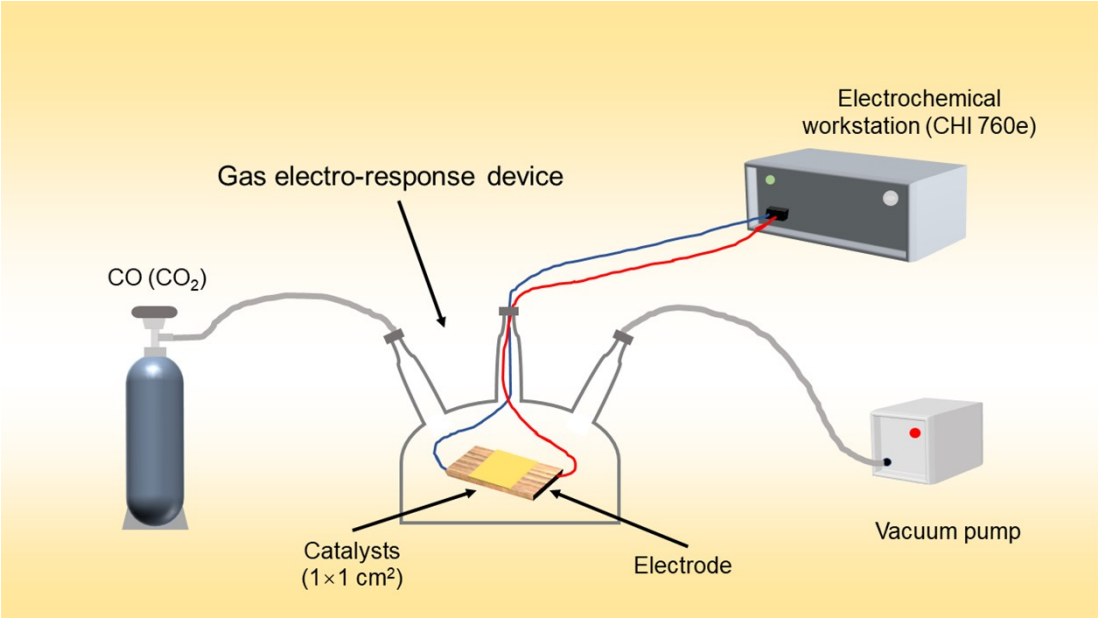

Figure S24. Schematic diagram of CO adsorption experiment.

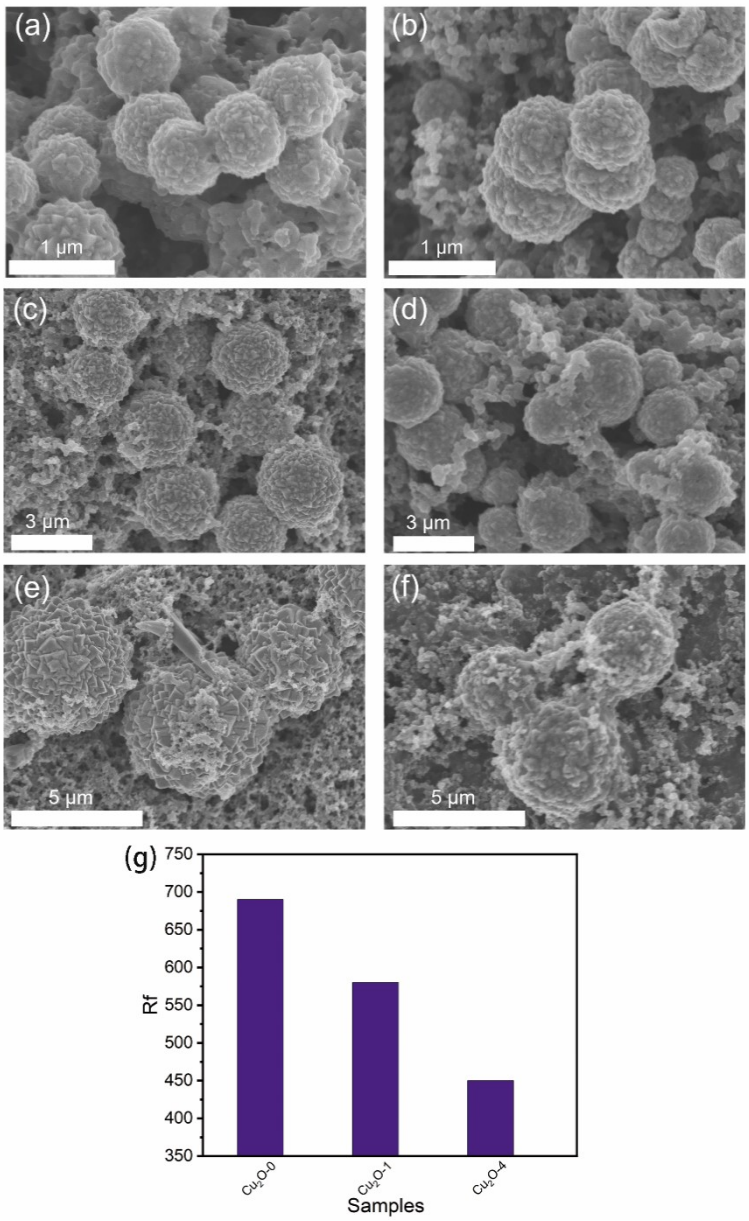

Figure S25. SEM images of Cu_2O-0 (a, b), Cu_2O-1 (c, d) and Cu_2O-4 (e, f) catalyst before and after CO_2RR; (g) the R_f of Cu_2O-0, Cu_2O-1 and Cu_2O-4 after CO_2RR.

From the Figure S25, the morphology of the Cu_2O-0 catalyst was almost unchanged before and after CO_2RR. However, the morphology of Cu_2O-1 and Cu_2O-4 changed before and after CO_2RR, and their cube corners became less pronounced after CO_2RR. Meanwhile, the Rf after CO_2RR of Cu_2O-1 and Cu_2O-4 also decreases significantly (Figure S25g). In summary, these factors may be the reason why the electrocatalytic CO_2 reduction performance and stability of Cu_2O-1 and Cu_2O-4 are not as good as Cu_2O-0.

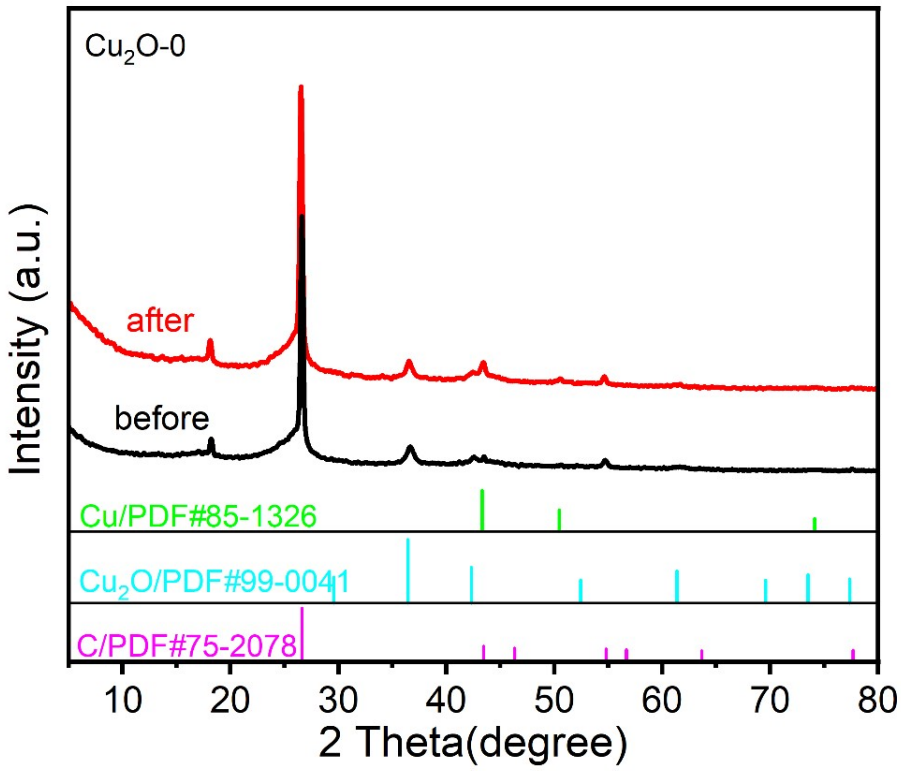

Figure S26. XRD patterns of Cu_2O-0 catalyst before and after CO_2RR.

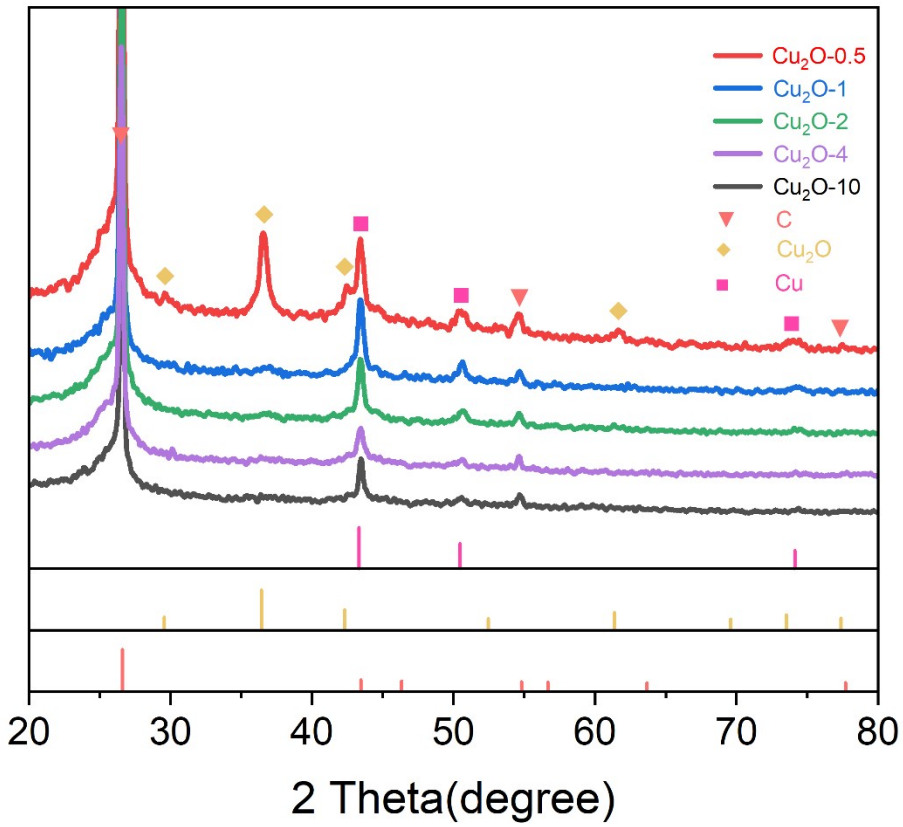

Figure S27. XRD patterns of Cu_2O-X catalyst after CO_2RR.

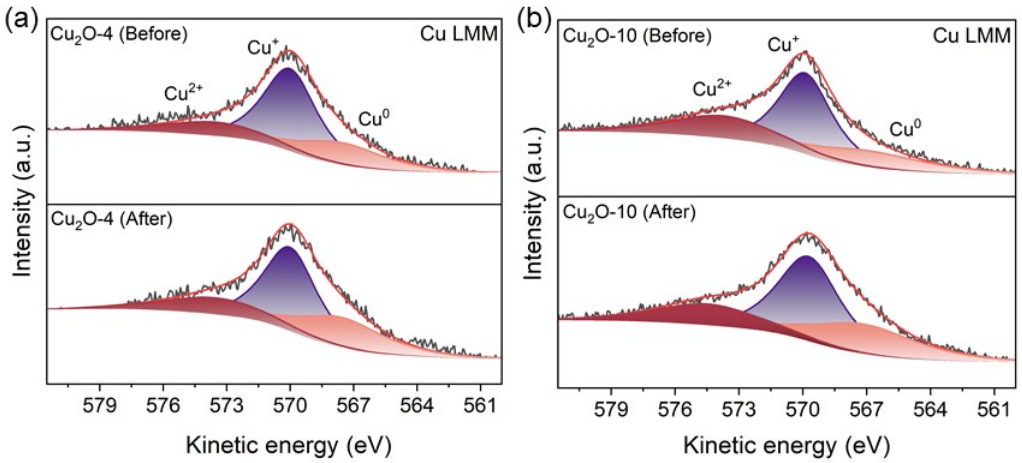

Figure S28. Deconvoluted Cu Auger LMM spectra of Cu_2O-X catalysts before and after CO_2RR. (a) Cu_2O-4. (b) Cu_2O-10.

The ratio of the Cu^0 fraction increased from 21.64% to 30.24%, and the ratio of the Cu^+ fraction decreased from 59.27% to 51.74% in the Cu_2O-4 catalyst. The ratio of Cu^0 component increased from 20.23% to 34.15% and the ratio of Cu^+ component decreased from 58.69% to 47.81% in Cu_2O-10 catalyst.

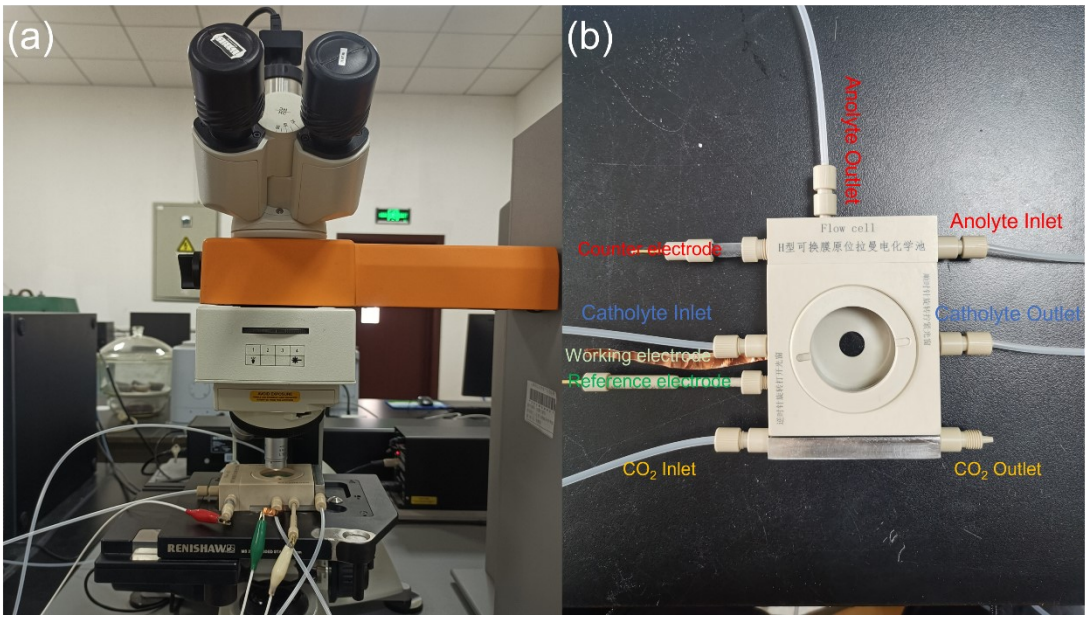

Figure S29. (a) Photo of a real electrochemical cell for in-situ Raman experiment setup. (b) Photo of electrolytic cell for in-situ Raman test.

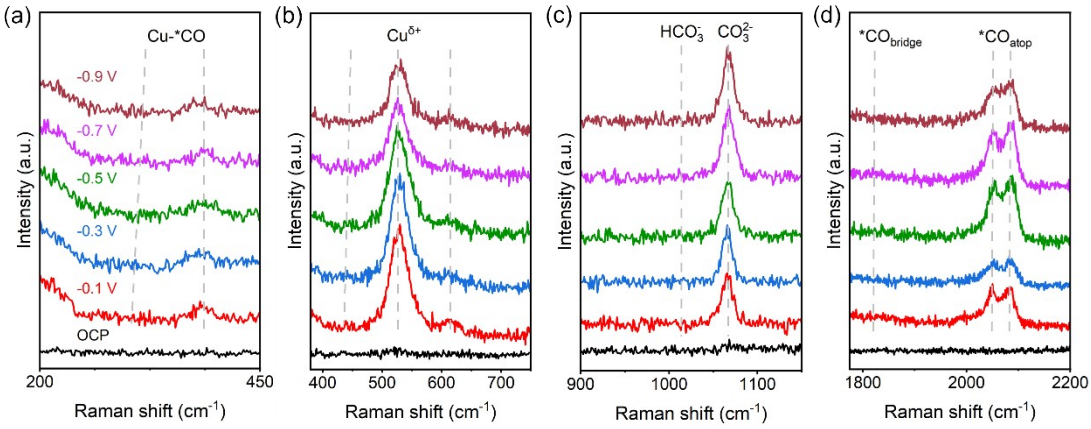

Figure S30. In-situ Raman spectra of Cu_2O-4 catalyst at various applied potentials (vs. RHE).

As shown in Figures S30b, with the increase of applied potential, the characteristic Cu^+ peaks (520 cm^{-1}) of the Cu_2O-4 catalyst were also preserved, the intensity of the peaks varied considerably, indicating that the valence state of Cu in the Cu_2O-4 catalyst was unstable, which was consistent with the results of the XRD (Figures S12 and 27) and XPS (Figure S28a) tests before and after CO_2RR of the Cu_2O-4 catalyst.

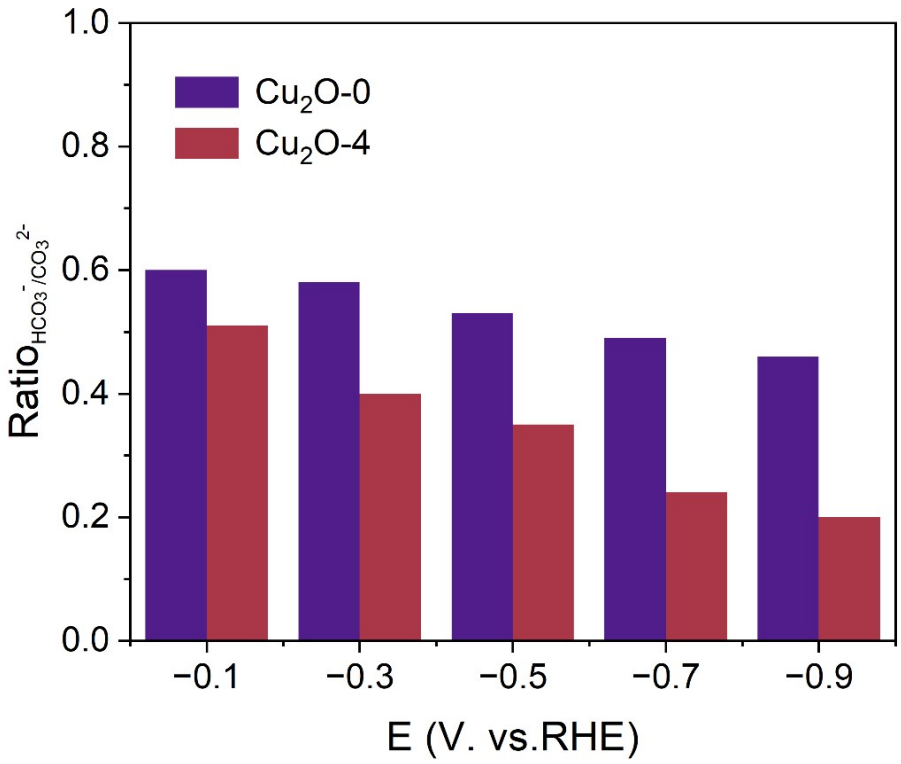

Figure S31. Ratio of HCO_3^-/CO_3^{2-} of Cu_2O-0 and Cu_2O-4 catalysts at various applied potentials.

Quantitative analysis of the characteristic peaks of HCO_3^- and CO_3^{2-} revealed that there was a slight decrease in the HCO_3^-/CO_3^{2-} values on the Cu_2O-0 catalyst with the increase of the applied potential, while the HCO_3^-/CO_3^{2-} values on the Cu_2O-4 catalyst decreased sharply.

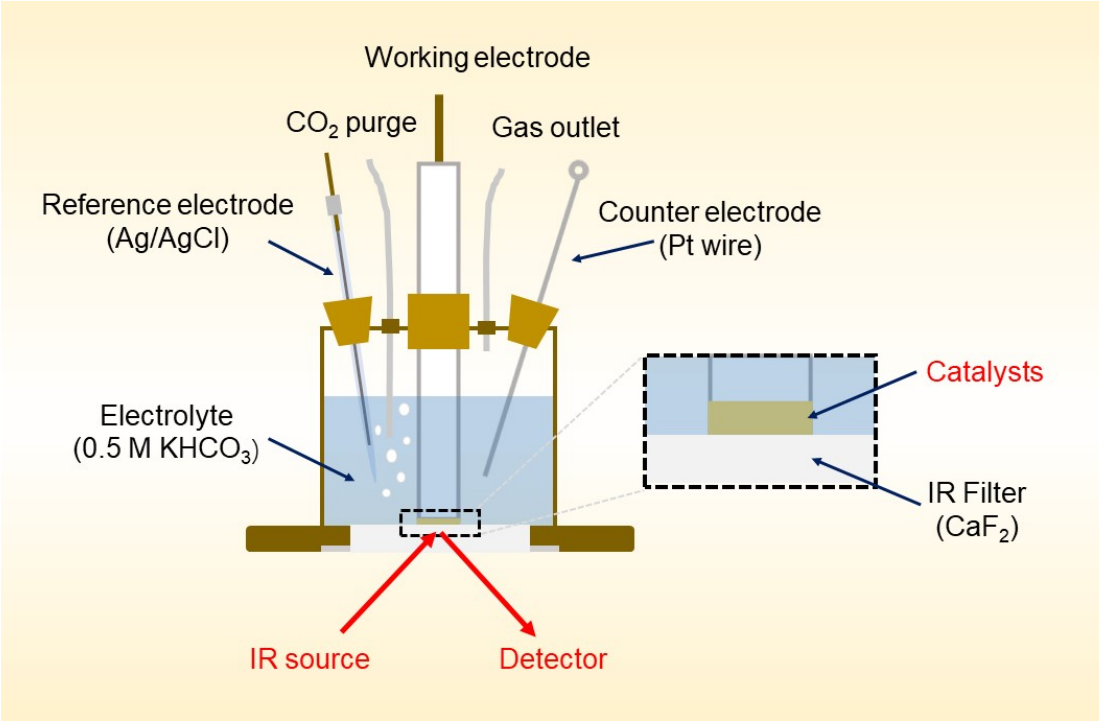

Figure S32. Schematic of electrolytic cell for in-situ FT-IR test.

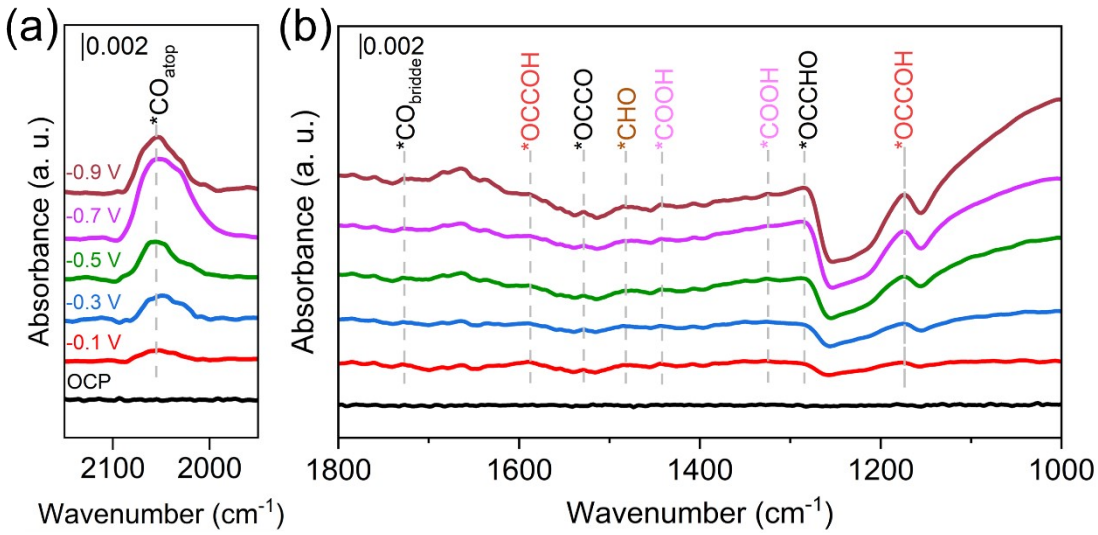

Figure S33. In-situ FTIR spectra of Cu_2O-4 catalyst at various applied potentials (vs. RHE).

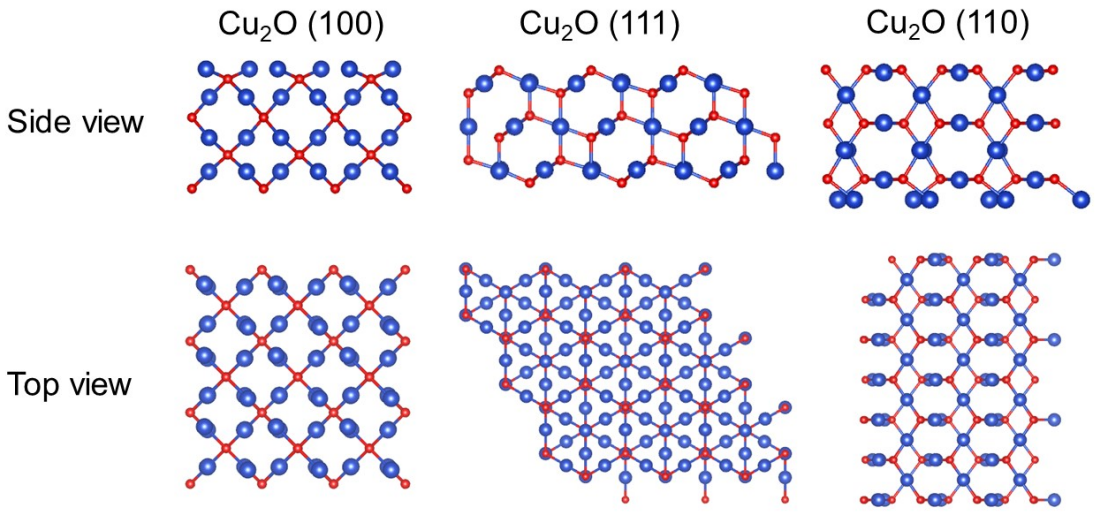

Figure S34. Side and top view of different Cu_2O configurations.

We obtained Cu_2O (100), Cu_2O (111) and Cu_2O (110) structure models by faceting Cu_2O unit cells, where Cu_2O (100), Cu_2O (111) and Cu_2O (110) structures contain 108, 162 and 162 atoms, respectively. When we optimize the structure, we optimize the K^+ adsorption structure as a whole, so as to select the thermodynamically stable structure. There is no specific adsorption method for K^+ on the Cu_2O surface, the distance from K^+ to each Cu_2O crystal plane is not the same, the structural model of each Cu_2O crystal plane has been given, and their distances can be measured in MS or VESTA software, for example, 2.432, 2.200, 2.400 Å are the distances from K^+ to Cu_2O (100), Cu_2O (111), Cu_2O (110) structural surfaces, respectively. When we optimize the structure, we do not consider the effect of solvation alone, but optimize the Cu_2O crystal planes that adsorb different K^+ as a whole. When the structure is optimized, the electron energy is obtained, then the corrected energy is calculated, and finally the two are added.

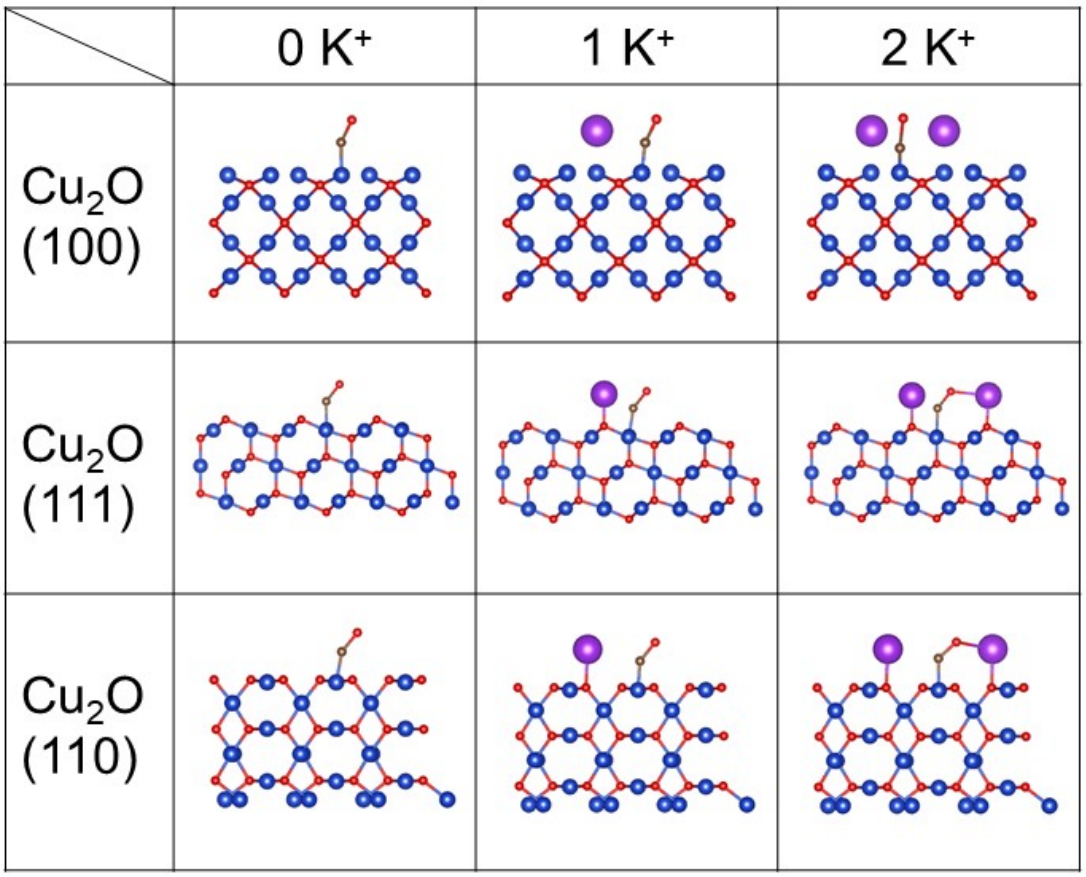

Figure S35. Schematic modeling of the adsorption of CO intermediates on three crystalline surfaces of Cu_2O (100), (111) and (110) at three K^+ concentrations of 0 K^+, 1 K^+ and 2 K^+, respectively.

When the K^+ concentration was 2, the K^+ on the surface of Cu_2O (111) and (110) crystals bonded not only with the oxygen atoms in Cu_2O but also with the oxygen atoms in *CO, which enhanced the adsorption capacity of *CO intermediates on the surface of Cu_2O (111) and (110) crystals.

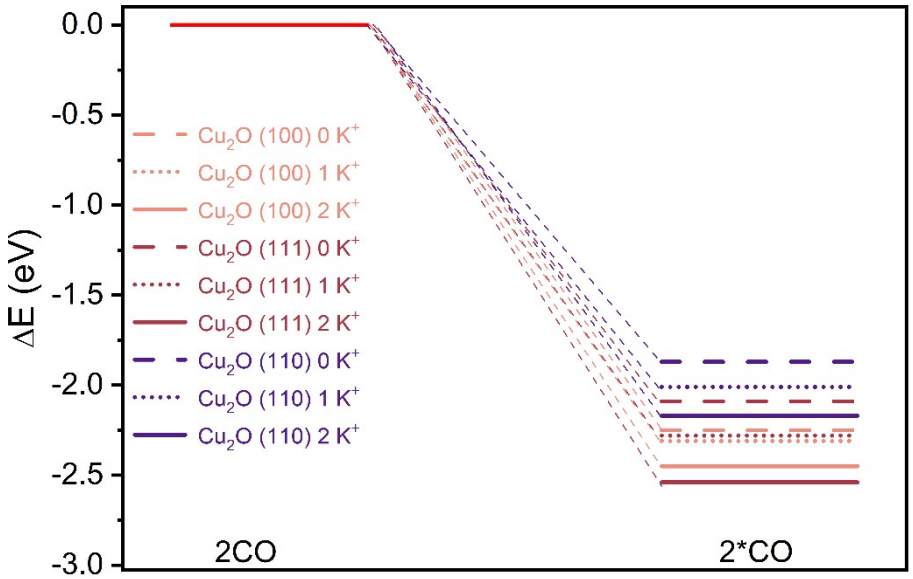

Figure S36. Adsorption energies of CO on three crystalline surfaces of Cu_2O (100), (111) and (110) at three K^+ concentrations of 0 K^+, 1 K^+ and 2 K^+, respectively.

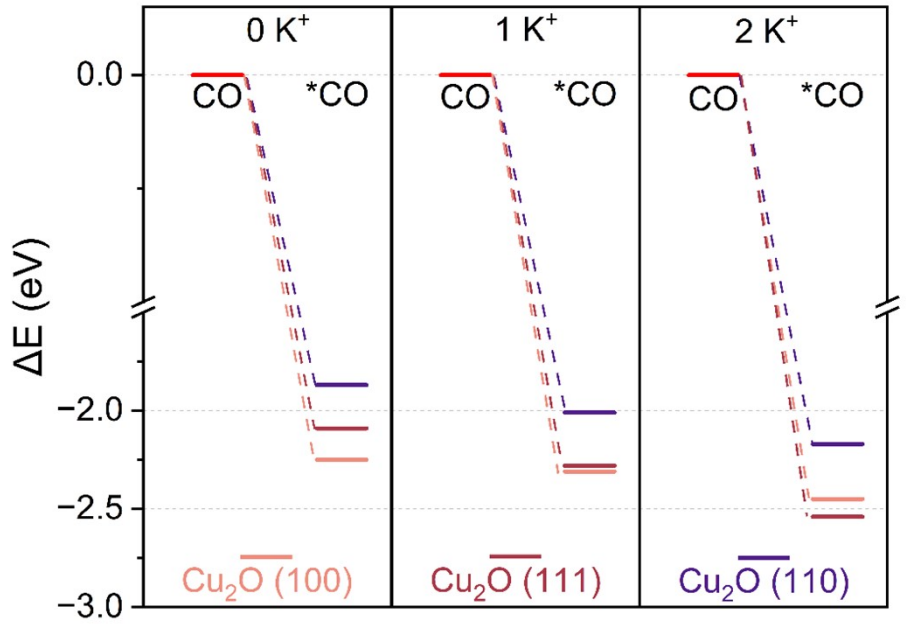

Figure S37. Comparison of adsorption energies of CO on three crystalline surfaces of Cu_2O (100), (111) and (110) at the same K^+ concentration.

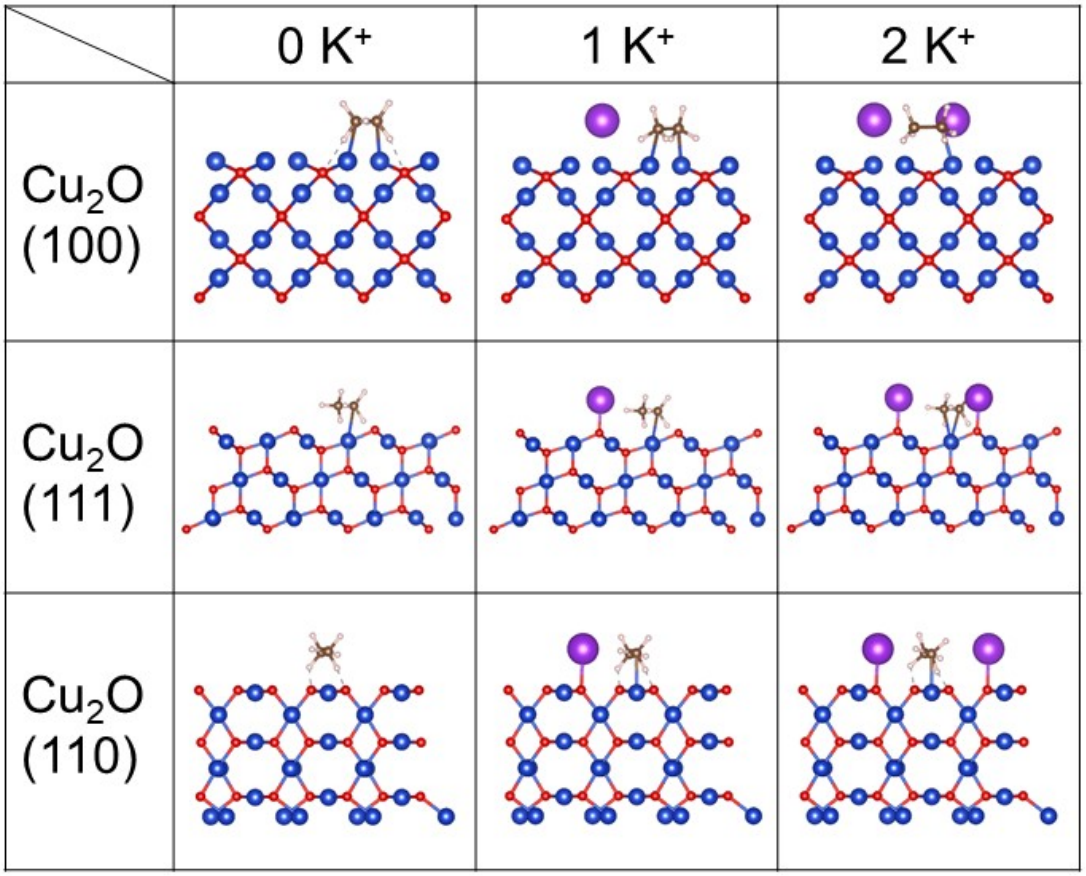

Figure S38. Schematic modeling of the adsorption of $*C_2H_4$ intermediates on three crystalline surfaces of Cu_2O (100), (111) and (110) at three K^+ concentrations of 0 K^+, 1 K^+ and 2 K^+, respectively.

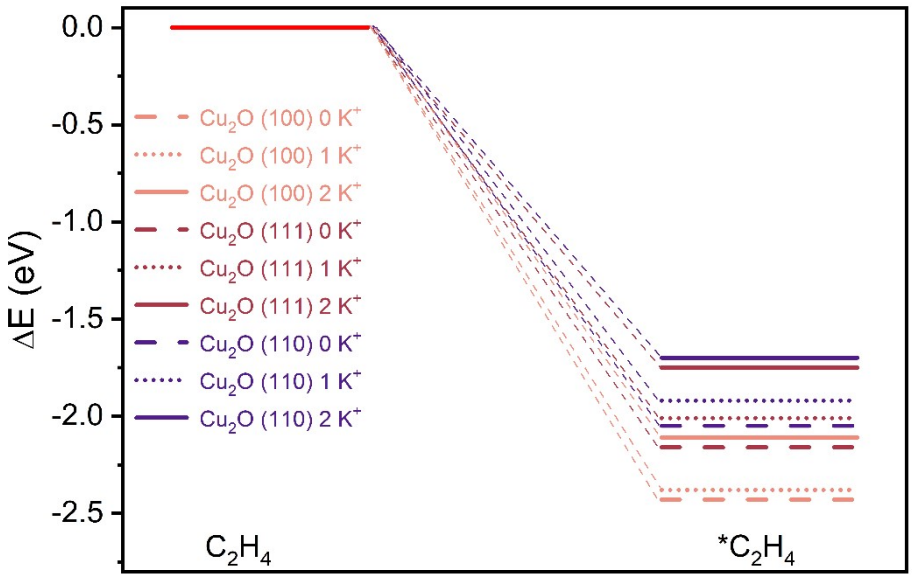

Figure S39. Adsorption energies of C_2H_4 on three crystalline surfaces of Cu_2O (100), (111) and (110) at three K^+ concentrations of 0 K^+, 1 K^+ and 2 K^+, respectively.

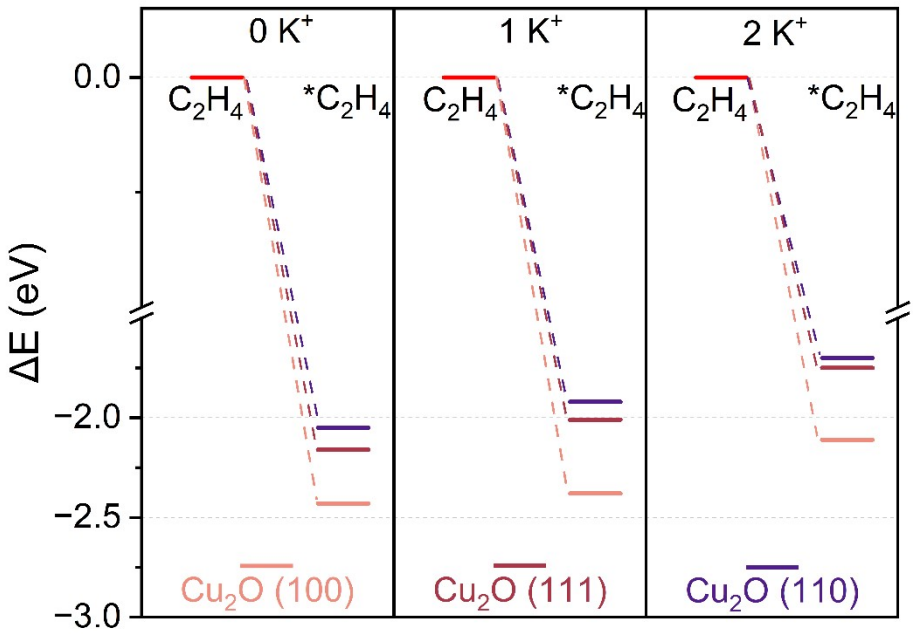

Figure S40. Comparison of adsorption energies of C_2H_4 on three crystalline surfaces of Cu_2O (100), (111) and (110) at the same K^+ concentration.

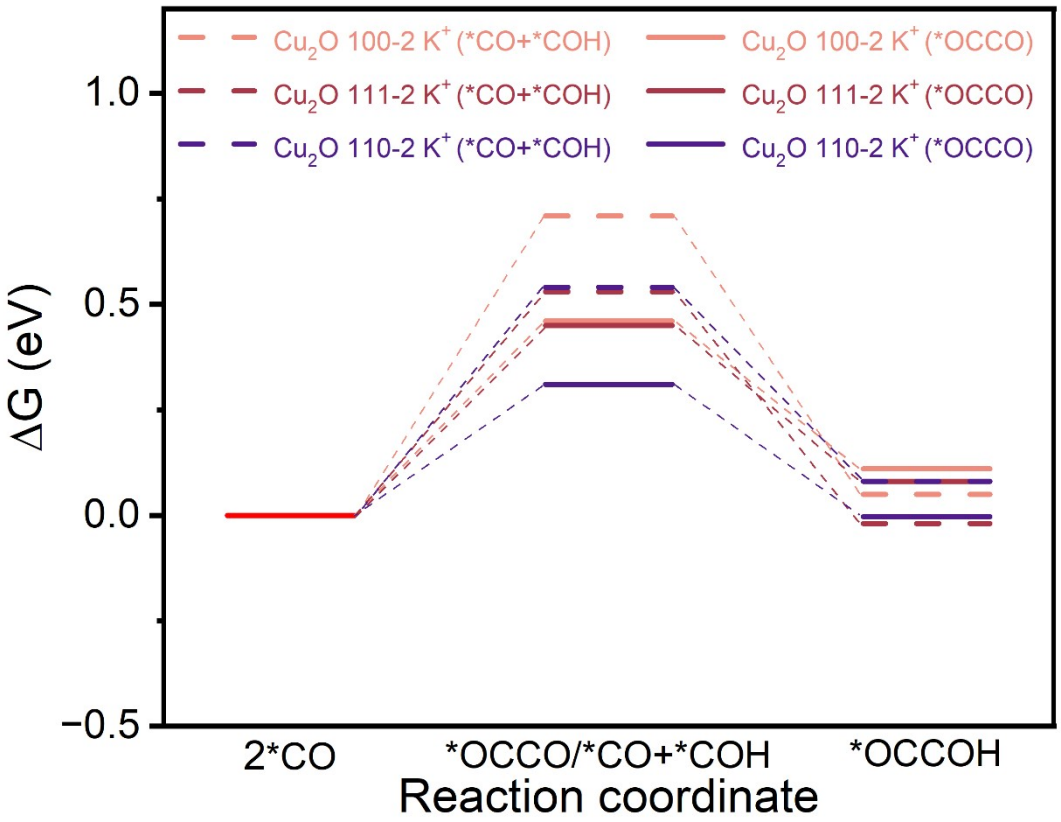

Figure S41. The free energy of C-C coupling with different paths.

There are two main ways for C-C coupling: ① 2 *CO →*OCCO → *OCCOH; ② 2 *CO → *CO+*COH → *OCCOH. We analyzed the free energy of different paths in C-C coupling using DFT calculations. From the Figure S41, it can be observed that the free energy of the C-C coupling path ① is lower than the free energy of the C-C coupling path ②, indicating that the C-C coupling path ① is more prone to occur.

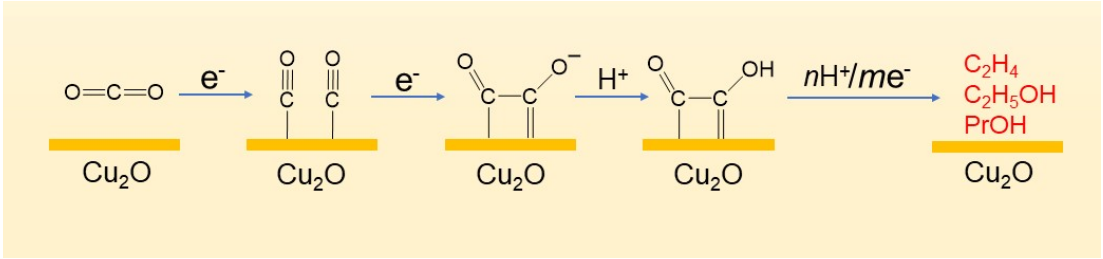

Figure S42. Reaction pathways for C_{2+} products in CO_2RR.

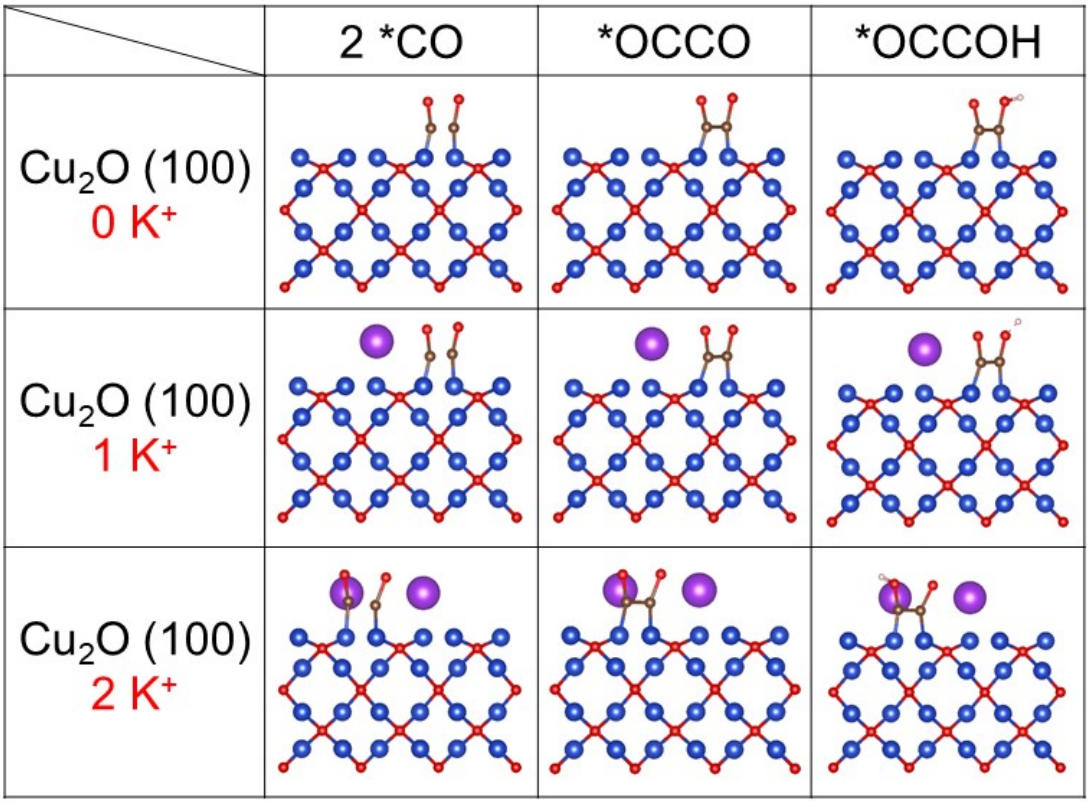

Figure S43. Schematic modeling of C-C coupling on the Cu_2O (100) crystal plane at three K^+ concentrations of 0 K^+, 1 K^+ and 2 K^+, respectively.

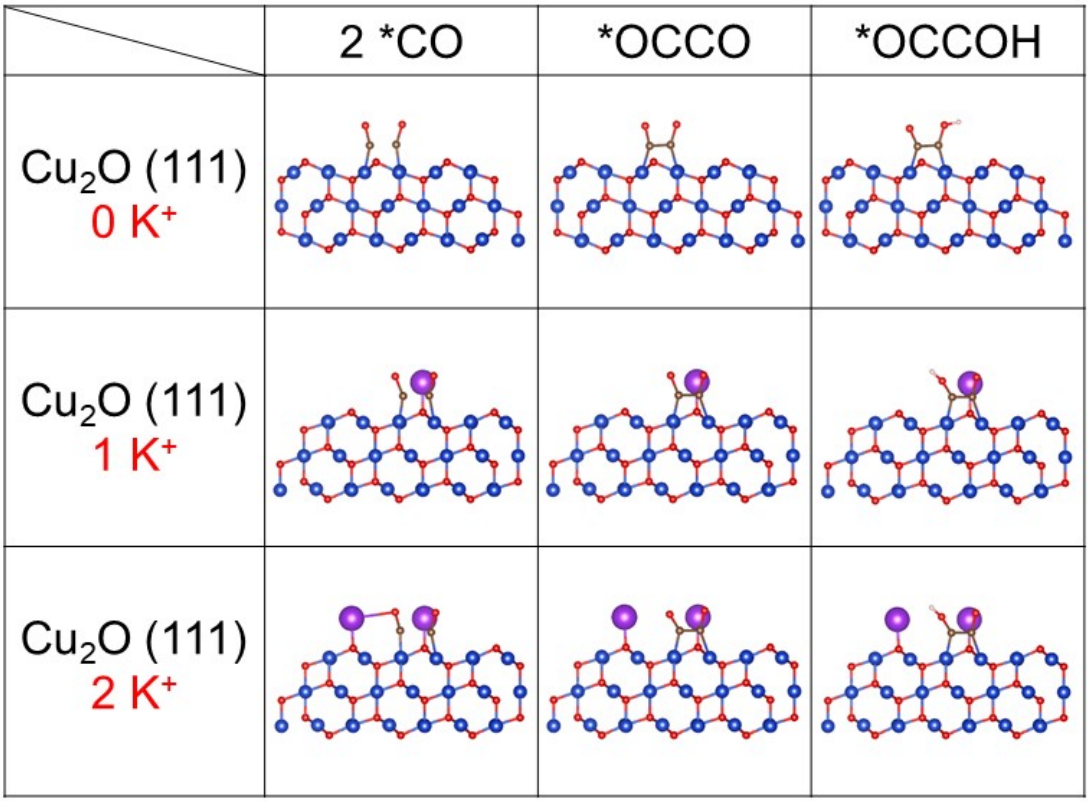

Figure S44. Schematic modeling of C-C coupling on the Cu_2O (111) crystal plane at three K^+ concentrations of 0 K^+, 1 K^+ and 2 K^+, respectively.

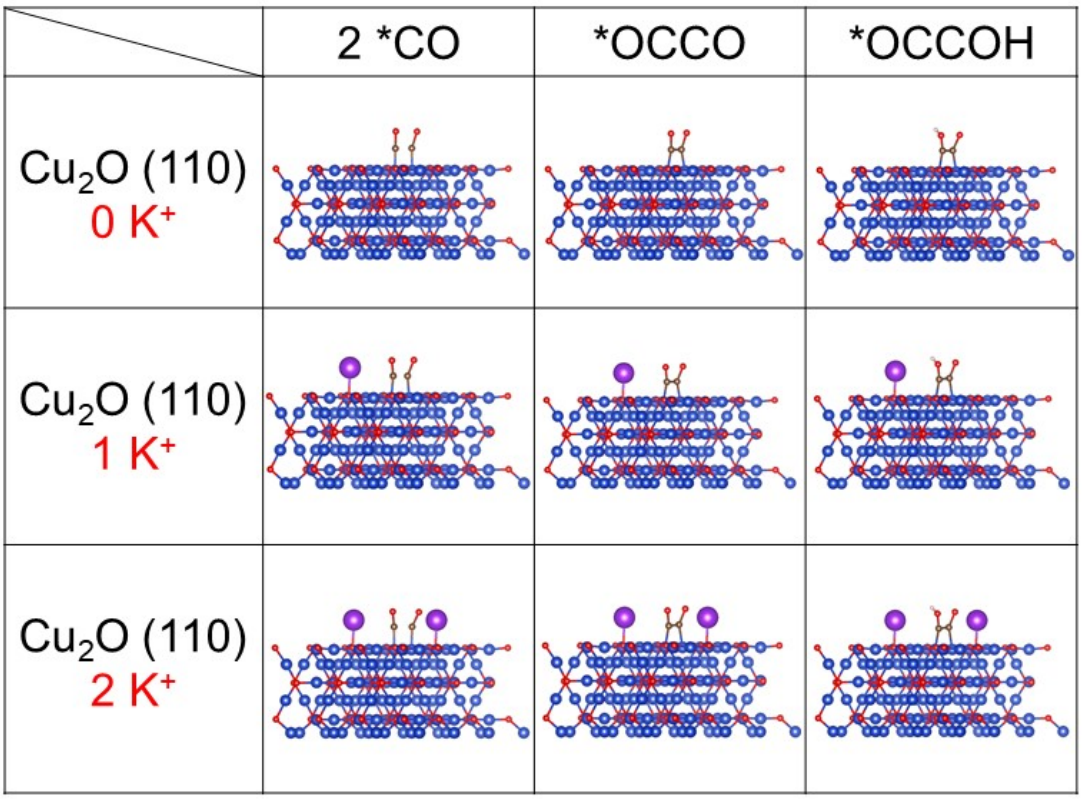

Figure S45. Schematic modeling of C-C coupling on the Cu_2O (110) crystal plane at three K^+ concentrations of 0 K^+, 1 K^+ and 2 K^+, respectively.

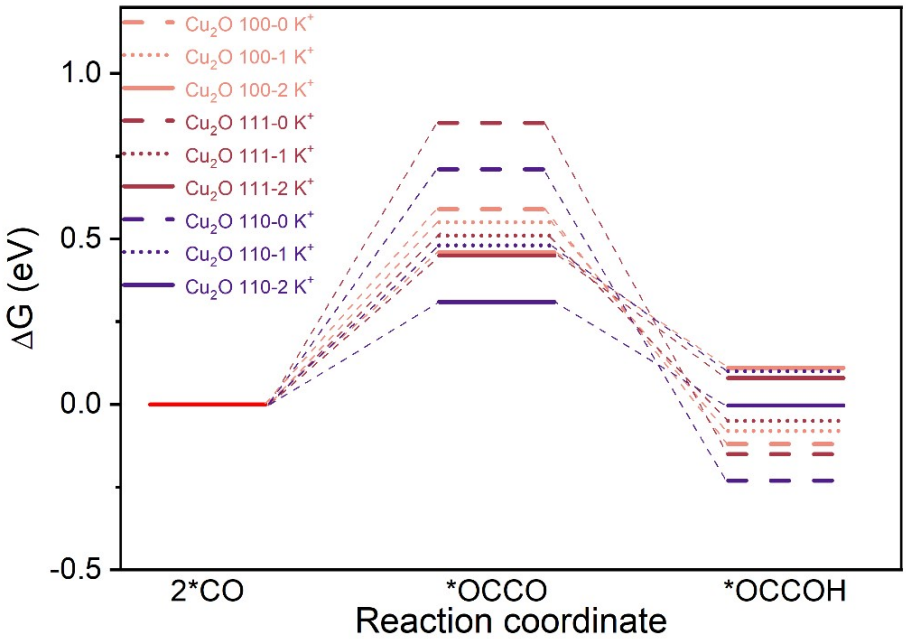

Figure S46. Gibbs free energy pathways for C-C coupling on three crystalline surfaces of Cu_2O (100), (111) and (110) at three K^+ concentrations of 0 K^+, 1 K^+ and 2 K^+, respectively.

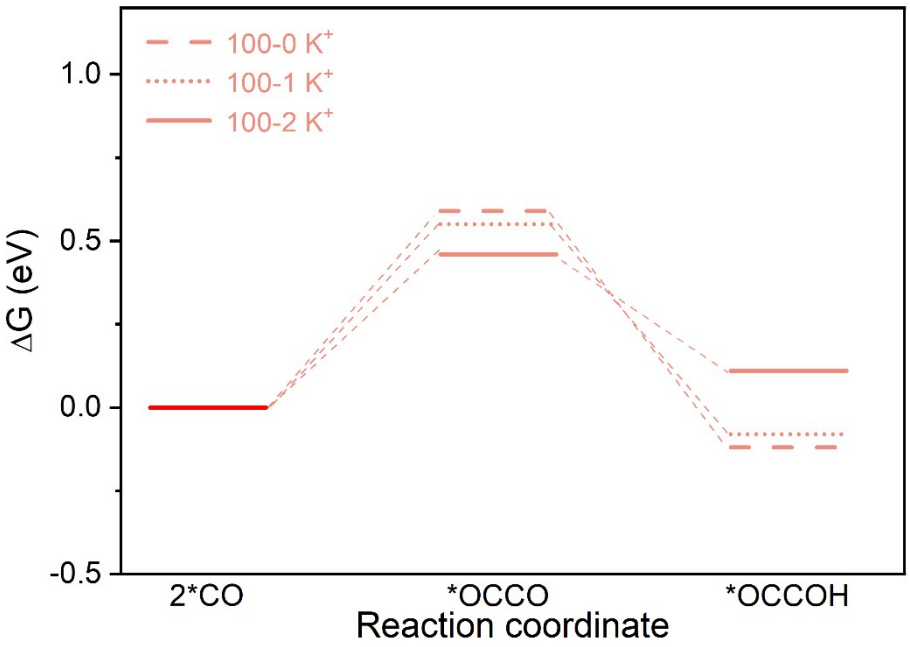

Figure S47. Gibbs free energy pathways for C-C coupling on Cu_2O (100) at three K^+ concentrations of 0 K^+, 1 K^+ and 2 K^+, respectively.

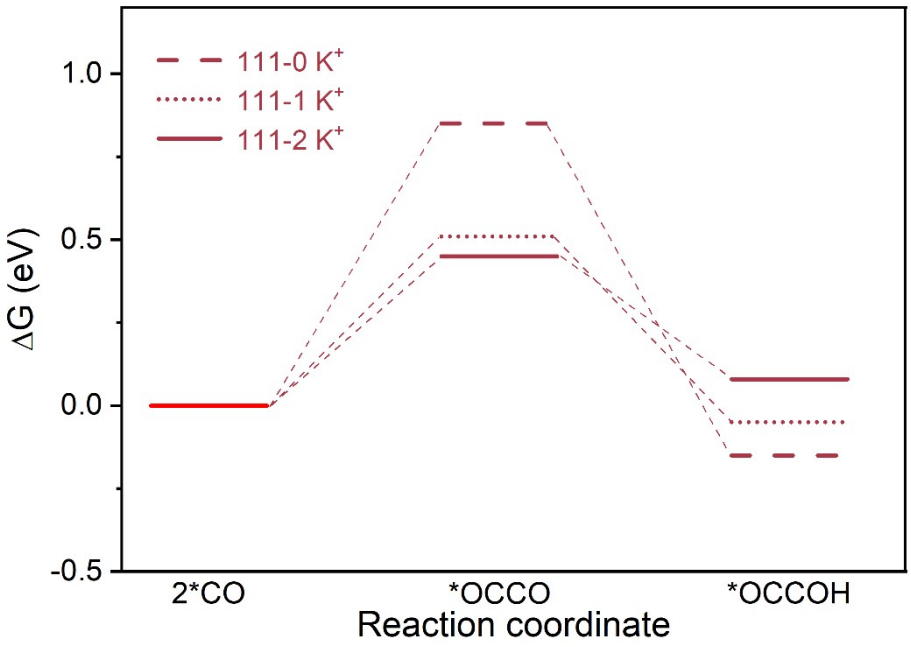

Figure S48. Gibbs free energy pathways for C-C coupling on Cu_2O (111) at three K^+ concentrations of 0 K^+, 1 K^+ and 2 K^+, respectively.

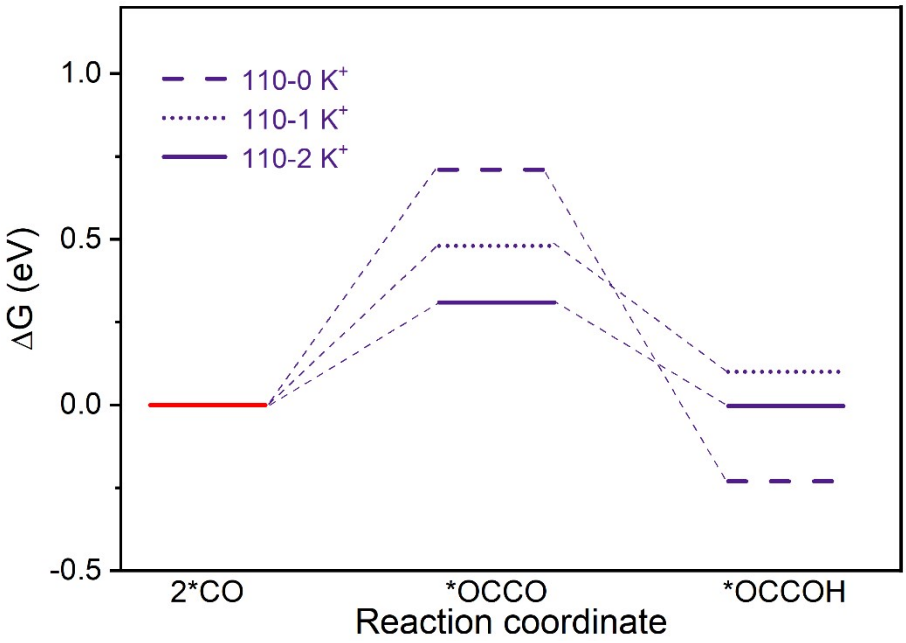

Figure S49. Gibbs free energy pathways for C-C coupling on Cu_2O (110) at three K^+ concentrations of 0 K^+, 1 K^+ and 2 K^+, respectively.

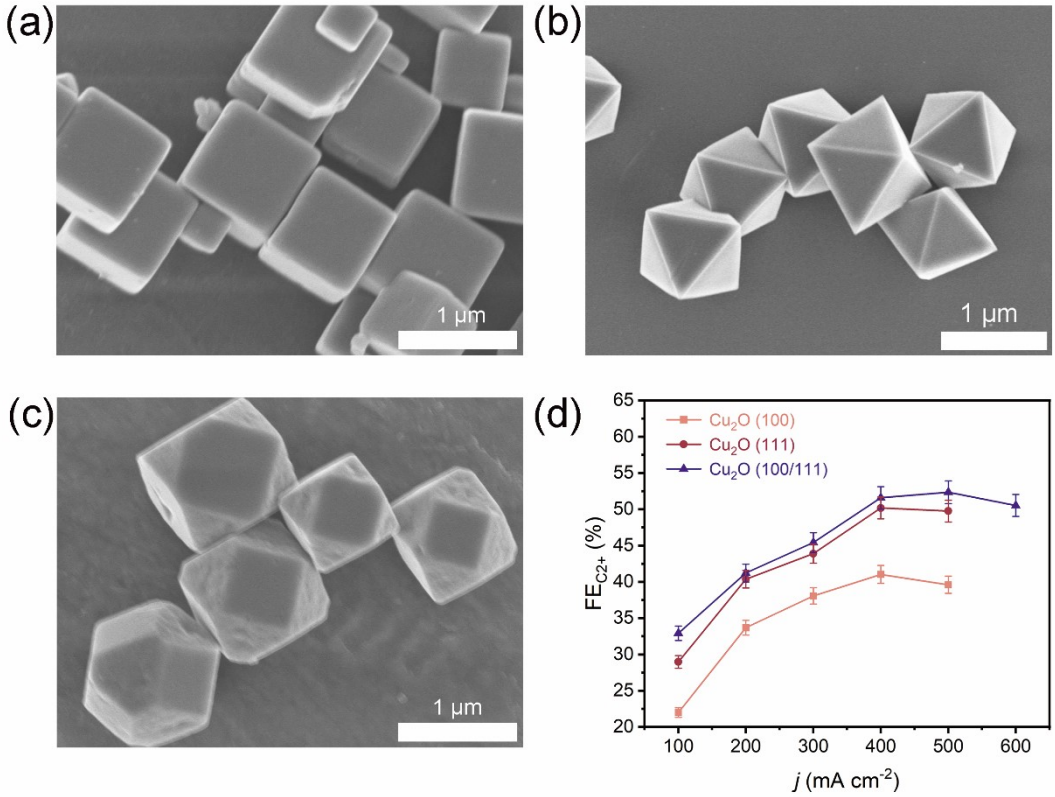

Figure S50. SEM images of Cu_2O (100) (a), Cu_2O (111) (b), and Cu_2O (100/111) (c). (d) the FE_{2+} of Cu_2O (100), Cu_2O (111) and Cu_2O (100/111).

To verify the effect of Cu_2O crystal planes on the electrocatalytic CO_2 reduction performance, we synthesized Cu_2O particles with different crystal planes, namely Cu_2O containing 100, 111, and 100/111 crystal planes.[18,19] At the same time, their electrocatalytic CO_2 reduction performance was studied. As shown in the Figure S50, Cu_2O containing 100, 111, and 100/111 crystal faces was successfully synthesized, and the FE sequence for producing C_{2+} products is Cu_2O (100/111) ＞ Cu_2O (111) ＞ Cu_2O (100). This result is consistent with our DFT calculation.

Table S1. Double layer capacitance (C_{dl}), surface roughness coefficient (R_f) and electrochemically active surface area (ECSA) of Cu_2O-X catalysts.

Samples	C_{dl} (mF cm^{-2})	R_f	ECSA (cm^2)
Cu_2O-0	42.8	713.33	713.33
Cu_2O-0.5	40.3	671.67	671.67
Cu_2O-1	39.6	660	660
Cu_2O-2	37.6	626.67	626.67
Cu_2O-4	33.1	551.67	551.67
Cu_2O-10	23.5	391.67	391.67

*R_f was estimated from the ratio of double-layer capacitance (C_{dl}) for the working electrode and the corresponding smooth polycrystalline Cu_2O electrode (60 μF cm^{-2}). ECSA = R_f × S, where S stands for the geometric area of the electrode (in this work, S = 1 cm^2).

Table S2. The K^+ adsorption data for Cu_2O-X catalysts.

Samples	Applied Potential (Vs. RHE)	Background (ug/ml)	K^+ Concentration (ug/ml)	K^+ concentration with deducted the background (ug/ml)
Cu_2O-0	-1.2	91.60	208.70	117.10
Cu_2O-0.5		82.71	173.43	90.72
Cu_2O-1		66.25	144.06	77.81
Cu_2O-2		109.57	167.50	57.93
Cu_2O-4		110.66	158.32	47.66
Cu_2O-10		122.29	147.83	25.54

Table S3. Adsorption energies of CO on three crystalline surfaces of Cu_2O (100), (111) and (110) at three K^+ concentrations of 0 K^+, 1 K^+ and 2 K^+, respectively.

CO Adsorption Energies (eV)	**0 K^+**	**1 K^+**	**2 K^+**
Cu_2O (100)	-2.25	-2.31	-2.45
Cu_2O (111)	-2.09	-2.28	-2.54
Cu_2O (110)	-1.87	-2.01	-2.17

The increase in K^+ concentration from 0 K^+ to 2 K^+ increased the adsorption energies of *CO intermediates on the three crystalline surfaces of Cu_2O (100) (111) and (110) by 0.2 eV, 0.45 eV, and 0.3 eV, respectively. The trend of increase was larger for Cu_2O (111) and (110) than that for Cu_2O (100) crystalline surfaces.

With the increase of K^+ concentration, the adsorption energy increment amount of the *CO intermediate on Cu_2O (111) and Cu_2O (110) crystallites was larger than that on Cu_2O (100) crystallites. The larger amount of energy increment suggests that, with more Cu_2O (111) and Cu_2O (110) crystalline surfaces and increasing K^+ concentration, this will promote C-C coupling during CO_2RR to produce more C_{2+} products.

Table S4. Adsorption energies of C_2H_4 on three crystalline surfaces of Cu_2O (100), (111) and (110) at three K^+ concentrations of 0 K^+, 1 K^+ and 2 K^+, respectively.

C_2H_4 Adsorption Energies (eV)	**0 K^+**	**1 K^+**	**2 K^+**
Cu_2O (100)	-2.43	-2.38	-2.11
Cu_2O (111)	-2.16	-2.01	-1.75
Cu_2O (110)	-2.05	-1.92	-1.70

Table S5. Gibbs free energy of C-C coupling and hydrogenation on three crystalline surfaces of Cu_2O (100), (111) and (110) at three K^+ concentrations of 0 K^+, 1 K^+ and 2 K^+, respectively.

G (eV)	**2*CO-to-*OCCO**			***OCCO-to-*OCCOH**		
	0 K^+	**1 K^+**	**2 K^+**	**0 K^+**	**1 K^+**	**2 K^+**
Cu_2O (100)	0.59	0.55	0.46	-0.12	-0.08	0.11
Cu_2O (111)	0.85	0.51	0.45	-0.15	-0.05	0.08
Cu_2O (110)	0.71	0.48	0.31	-0.23	0.1	-0.003

Section 5. References

1. D. S. Chen, W. B. Yu, Z. Deng, J. Liu, J. Jin, Y. Li, M. Wu, L. H. Chen and B. L. Su, *RSC Adv.*, 2015, **5**, 55520-55526.
2. P. S. Li, J. H. Bi, J. Y. Liu, Y. Wang, Kang, C. X. X. F. Sun, J. L. Zhang, Z. M. Liu, Q. G. Zhu and B. X. Han, *J. Am. Chem. Soc.*, 2023, **145**, 4675-4682.
3. B. Chi, H. Lin, J. B. Li, N. Wang and J. Yang, *Int. J. Hydrogen Energ.*, 2006, **31**, 1210-1214.
4. B. Chi, H. Lin and J. B. Li, *Int. J. Hydrogen Energ.*, 2008, **33**, 4763-4768.
5. A. Laszczyńska, I. Szczygieł, *Int. J. Hydrogen Energ.*, 2020, **45**, 508-520.
6. Y. J. Zhou, Y. Q. Liang, J. W. Fu, K. Liu, Q. Chen, X. Q. Wang, H. M. Li, L. Zhu, J. H. Hu, H. Pan, M. Miyauchi, L. X. Jiang, E. Cortés and M. Liu, *Nano Lett.*, 2022, **22**, 1963-1970.
7. B. P. Yang, K. Liu, H. Jing, W. Li, C. X. Liu, J. W. Fu, H. M. Li, J. E. Huang, P. F. Ou, T. Alkayyali, C. Cai, Y. X. Duan, H. Liu, P. An, N. Zhang, W. Z. Li, X. Q. Qiu, C. K. Jia, J. H. Hu, L. Y. Chai, Z. Lin, Y. L. Gao, M. Miyauchi, E. Cortés, S. A. Maier and M. Liu, *J. Am. Chem. Soc.*, 2022, **144**, 3039-3049.
8. G. Kresse, J. Hafner, *Phys. Rev. B*, 1993, **47**, 558-561.
9. G. Kresse, J. Hafner, *Phys. Rev. B*, 1994, **49**, 14251-14269.
10. J. P. Perdew, K. Burke and M. Ernzerhof, *Phys. Rev. Lett.*, 1996, **77**, 3865-3868.
11. G. Kresse, D. Joubert, *Phys. Rev. B*, 1999, **59**, 1758-1775.
12. P. E. Blöchl, *Phys. Rev. B*, 1994, **50**, 17953-17979.
13. J. K. Nørskov, J. Rossmeisl, A. Logadottir, L. Lindqvist, J. R. Kitchin, T. Bligaard and H. Jonsson, *J. Phys. Chem. B*, 2004, **108**, 17886-17892.
14. L. I. Bendavid, E. A. Carter, *J. Phys. Chem. C*, 2013, **117**, 26048-26059.
15. K. Jiang, R. B. Sandberg, A. J. Akey, X. Liu, D. C. Bell, J. K. Norskov, K. Chan and H. Wang, *Nat. Catal.*, 2018, **1**, 111-119.
16. P. P. Yang, X. L. Zhang, F. Y. Gao, Y. R. Zheng, Z. Z. Niu, X. Yu, R. Liu, Z. Z. Wu, S. Qin, L. P. Chi, Y. Duan, T. Ma, X. S. Zheng, J. F. Zhu, H. J. Wang, M. R. Gao, S. H. Yu and J. Am, *Chem. Soc.*, 2020, **142**, 6400-6408.
17. P. S. Li, J. H. Bi, J. Y. Liu, Y. Wang, X. C. Kang, X. F. Sun, J. L. Zhang, Z. M. Liu, Q. G. Zhu and B. X. Han, *J. Am. Chem. Soc.*, 2023, **145**, 4675-4682.
18. Y. G. Gao, Q. Wu, X. Z. Liang, Z. Y. Wang, Z. K. Zheng, P. Wang, Y. Y. Liu, Y. Dai, M-H.

Whangbo and B.B. Huang, *Adv. Sci*., 2020, **7**, 1902820.

19. Z-Y. Zhang, H. Tian, H. Jiao, X. Wang, L. Bian, Y. Liu, N. Khaorapapong, Y. Yamauchi and Z-L. Wang, *J. Mater. Chem. A*., 2024, **12**, 1218-1232.